Missouri State University

BearWorks

MSU Graduate Theses

Spring 2016

Molecule Assisted Hydrothermal Synthesis Of Zinc Oxide Nanomaterials With Possible Applicatios In Solar Energy

Austin Major Shearin

As with any intellectual project, the content and views expressed in this thesis may be considered objectionable by some readers. However, this student-scholar's work has been judged to have academic value by the student's thesis committee members trained in the discipline. The content and views expressed in this thesis are those of the student-scholar and are not endorsed by Missouri State University, its Graduate College, or its employees.

Follow this and additional works at: https://bearworks.missouristate.edu/theses

 Part of the Materials Science and Engineering Commons

Recommended Citation

Shearin, Austin Major, "Molecule Assisted Hydrothermal Synthesis Of Zinc Oxide Nanomaterials With Possible Applicatios In Solar Energy" (2016). *MSU Graduate Theses*. 2377.
https://bearworks.missouristate.edu/theses/2377

This article or document was made available through BearWorks, the institutional repository of Missouri State University. The work contained in it may be protected by copyright and require permission of the copyright holder for reuse or redistribution.
For more information, please contact BearWorks@library.missouristate.edu.

MOLECULE ASSISTED HYDROTHERMAL SYNTHESIS OF ZINC OXIDE NANOMATERIALS WITH POSSIBLE APPLICATIONS IN SOLAR ENERGY

A Masters Thesis

Presented to

The Graduate College of

Missouri State University

In Partial Fulfillment

Of the Requirements for the Degree

Master of Science, Materials Science

By

Austin Major Shearin

May 2016

Copyright 2016 by Austin Major Shearin

MOLECULE ASSISTED HYDROTHERMAL SYNTHESIS OF ZINC OXIDE NANOMATERIALS WITH POSSIBLE APPLICATIONS IN SOLAR ENERGY

Physics, Astronomy, and Materials Science

Missouri State University, May 2016

Master of Science

Austin Major Shearin

ABSTRACT

A molecule assisted hydrothermal synthesis of zinc oxide nanomaterials with L-lysine has been performed to understand the interaction between the biomolecule and the zinc oxide structures during synthesis. The molecule alters the growth kinetics during the formation of the nanomaterials in the hydrothermal reaction. This alters the size and shape of the materials as seen in the scanning electron microscope. X-ray diffraction results confirm the hexagonal Wurtzite structure that zinc oxide forms and indicates no other phases in the nanomaterial. The lattice parameters are not altered, but the atomic percentage of zinc to oxygen within the structure changes as analyzed by Topas crystallography software. Energy dispersive x-ray spectroscopy and x-ray photoelectron spectroscopy both confirm a larger concentration of oxygen atoms on the surface. No other atoms are detected, indicating little contamination in the samples and no lysine is present after cleaning the samples. Raman spectroscopy indicates the enhancement of the A_1(TO) mode in samples prepared with lysine. Ultraviolet-visible spectroscopy indicates a decreased energy band gap and increased concentration of defect energy level states significantly enhancing its optical absorption characteristics. Photoluminescence spectroscopy displays a slight red shift in the defect energy state peak for zinc oxide. These results indicate the possibility of using lysine as a treatment to enhance zinc oxides ability to be used as a solar absorbing medium in solar energy applications.

KEYWORDS: zinc oxide, hydrothermal, solar energy, nano-bio interaction, crystal structure, electronic structure

This abstract is approved as to form and content

_____

Dr. Kartik Ghosh
Chairperson, Advisory Committee
Missouri State University

MOLECULE ASSISTED HYDROTHERMAL SYNTHESIS OF ZINC OXIDE NANOMATERIALS WITH POSSIBLE APPLICATIONS IN SOLAR ENERGY

By

Austin Major Shearin

A Masters Thesis
Submitted to the Graduate College
Of Missouri State University
In Partial Fulfillment of the Requirements
For the Degree of Masters of Science, Materials Science

May, 2016

Approved:

_____
Dr. Kartik Ghosh, Chairperson

_____
Dr. Mahua Biswas, Member

_____
Dr. David Cornelison, Member

_____
Dr. Adam Wanekaya, Member

_____
Dr. Julie Masterson, Dean, Graduate College

ACKNOWLEDGEMENTS

I would like to thank Dr. Kartik Ghosh for his time as my research advisor, professor, and mentor. He has provided me with the knowledge I now possess that I feel will help me succeed in all of my future endeavors in the research and development career field.

I would also like to thank all of the other professors I have had in the Physics, Astronomy, and Materials Science Department. They have educated me so much in all the courses I have taken and I appreciate their effort in helping me in my studies immensely.

I would like to thank all of my colleagues I have had through my experience at Missouri State University. They are the true reason the university experience has been a successful one.

Lastly, I would like to thank my soon to be wife, Molli. She has been immensely helpful these past couple of months preceding the completion of this thesis. She is the reason I have been able to push myself to achieve all that I have.

TABLE OF CONTENTS

LIST OF TABLES

LIST OF FIGURES

INTRODUCTION

Basics of Nanomaterials

Nanomaterials are of significant importance as they are the next technological step in our society of smaller, lighter, faster, and more energy efficient. Nanomaterials are defined as any material with at least one length less than 100 nanometers (nm), where one nanometer is one billionth of a meter. Their extremely small size brings rise to quantum effects that can alter the materials physical, optical, thermal, and electrical properties to be drastically different than their counter part bulk material. These changes in properties must be understood before this whole new field of materials can be implemented into the commercial industry.

Materials research has been focused on nanomaterials for some time now. There are many different ways of synthesizing these different nanomaterials. The simplest process is called milling and is the mechanical grinding or cutting of materials into smaller and smaller pieces. This process has been used to generate nano-pieces of graphite down to 10 nm size[1]. A more advanced synthesis technique is the sol-gel method where a colloidal solution of materials is formed into a gel, heated to remove the solvent, and sintered to create a powdered structure. An example of this process has been used to synthesize copper oxide nanoparticles in a silica matrix[2].

Nanomaterials can be used in a plethora of applications. In the biomedical field, nanoparticles can be used for highly targeted and controlled release of drugs into the body[3], quantum dot fluorescence for fluorescence tagging in cell cultures[4], and magnetic nanoparticles used to enhance magnetic resonance imaging[5]. In the energetics field,

hollow shell nanoparticles are used in energy storage[6] and carbon nanotubes are a new electrode material in batteries[7].

One particular use for nanomaterials is as a new type of solar absorbing medium. For the best solar absorbing materials, the energy band of the material needs to be tuned to absorb the greatest amount of solar light as possible. The energy bands of nanoparticles can be altered by merely changing the size and structure or through doping. Tailoring the absorption characteristics of these materials becomes a process of altering the synthesis parameters and thus creating many new options for solar materials.

Zinc oxide (ZnO) was one of the first materials to be postulated as a solar material, but its instability and low efficiency made it lose out to silicon as the main commercialized solar absorption material. With the advances in nanomaterial science though, zinc oxide is being investigated again as a possible material for solar applications. It's being investigated in the integration into dye sensitized solar cells[8], in hybrid polymer solar cells[9], and as an electron transport buffer layer in organic solar cells[10] for example.

Zinc Oxide

Zinc oxide is a direct wide band gap material that crystallizes in the hexagonal wurtzite structure. It is currently being researched in many different applications such as light emitting diodes[11,12], gas sensors[13–15], biosensors[16,17], and piezoelectric electronics[18,19]. Zinc oxide is intrinsically an n-type conductor, but recent research has been able to demonstrate p-type conductivity. This new research has resurfaced the idea of using Zinc oxide as a solar absorbing material.

Structure. Zinc oxide can form in the crystalline structure of hexagonal wurtzite, zinc blende, or rock salt structure. At room temperature and atmospheric pressure, hexagonal wurtzite is the most favorable structure as it has the lowest energy. The hexagonal wurtzite structure of zinc oxide has lattice constants of a=0.3296 nm and c=0.52065 nm. In the hexagonal wurtzite structure, seen in Figure 1, each cation (zinc) has four tetrahedrally bonded anions (oxygen) surrounding it and vice versa for the anions. The bonding is shared between sp^3 covalent and ionic character[20]. The structure lacks inversion symmetry which gives rise to its piezoelectric and pyroelectric properties. The crystal structure also has polar surfaces between the positively charged Zn atoms and negatively charged oxygen atoms[21].

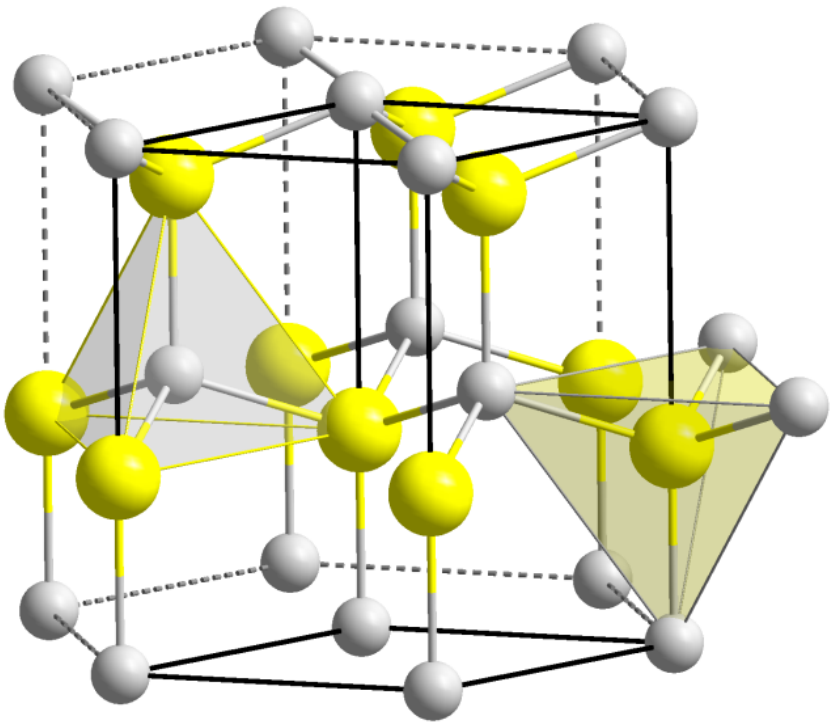

Figure 1: Hexagonal wurtzite crystal structure demonstrating tetrahedron bonding[22].

Nano-Sized Shapes and Structures. Zinc oxide nanostructures can be synthesized in solution or a gaseous phase. The many types of gaseous phase synthesis include vapor phase transport[23], physical vapor deposition[24], and thermal oxidation[25]. The solution based deposition includes zinc acetate sol-gel method[26], template assisted growth[27], electrophoresis[28] and solvothermal synthesis[29]. The gaseous phase is more expensive so the solution based synthesis is more popular[21].

Through the liquid phase synthesis of zinc oxide nanoparticles, many different sizes and shapes are possible by varying the different growth parameters such as pH, temperature, time, and precursor material and concentration[30]. Zinc oxide nanorods[31], nanocombs[32], nanorings[33], nanoloops[34], nanobelts[35], and nanocages[36] have all been produced through liquid phase synthesis. These different structures are possible to achieve by altering the growth kinetics which thereby alter the growth behavior. The facet with the lowest energy has the largest surface area in the structure and vice versa for the facet with the highest energy[37].

Modes of Vibration. Zinc oxide has six optical phonon modes at the Brillouin zone. The phonon modes are $1A_1$, $1E_1$, $2B_1$, and $2E_2$[38]. The $2B_1$ modes are both Raman and infrared inactive while the other phonon modes are all Raman active. The E_2 vibrational mode has two different frequencies as one is associated with the zinc lattice and the other with the oxygen lattice[39]. The zinc lattice is associated with the E_{2L} and the oxygen lattice with the E_{2H} phonon mode. The A_1 and E_1 modes are polar so they split into transverse optical (TO) and longitudinal optical (LO) parts with different frequencies[40]. These four Raman active modes are displayed in Figure 2. The A_1 mode is

a c-axis vibration and the E_1 and E_2 modes are x-y plane vibrations so distinguishing between the two can give information about the crystal in the direction of the vibration.

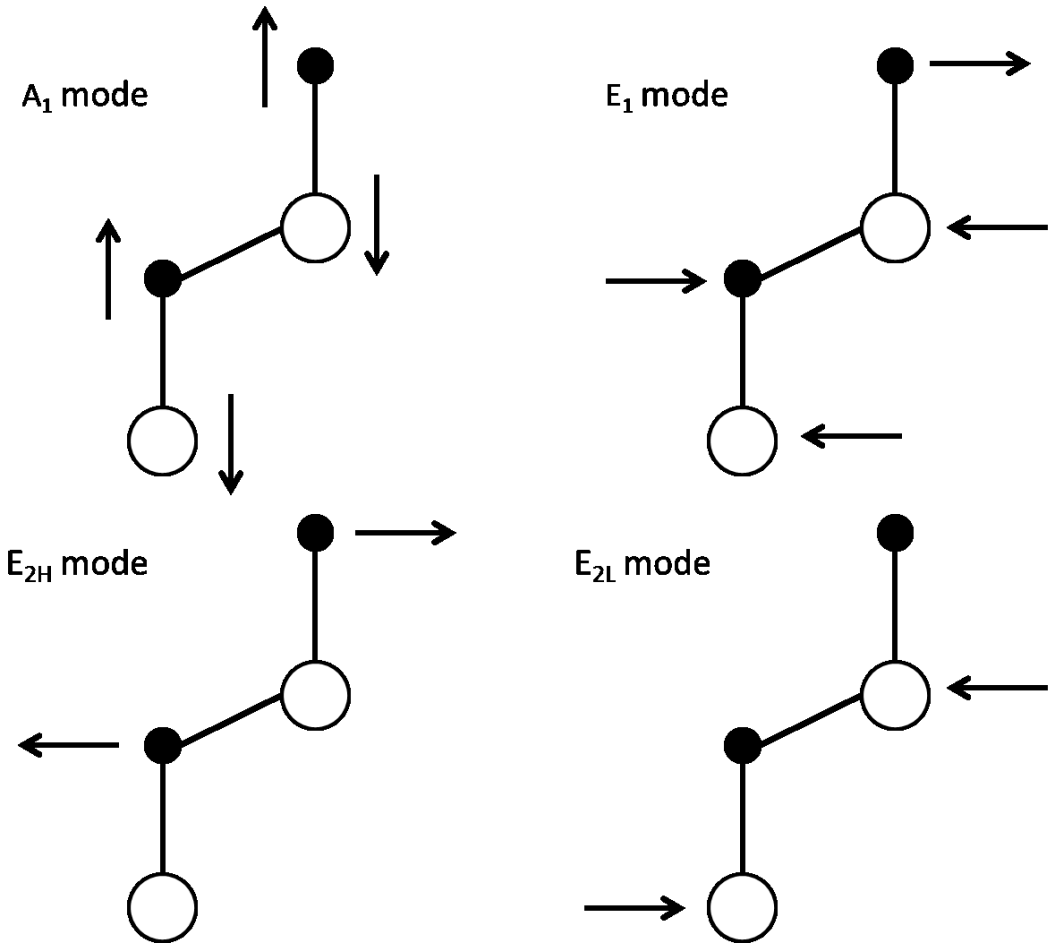

Figure 2: Raman active modes of vibration in the hexagonal wurtzite structure of zinc oxide with arrows representing the oscillatory direction of the vibration.

Defects in Crystal Structure. There are both intrinsic and extrinsic forms of defects in defects in crystal structures. There are point, line, and planar defects when looking at crystals. Line and planar defects do not play as big a role in nanomaterials due to their small size, but point defects in a nanomaterial can drastically alter its properties. Of the point defects, there are vacancies, interstitials, and substitutions. Vacancies are missing

atoms in the lattice, interstitials are atoms in the empty spots in the lattice between atoms, and substitutions are substitutions of atoms for others.

Figure 3 displays these different kinds of defects.

Zinc oxide has intrinsic defects that are prevalent in all samples. These point defects are oxygen vacancies, zinc interstitials, and hydrogen interstitials[41]. There are more that arise by changing the growth parameters of zinc oxide to encourage intrinsic defects that include zinc vacancies, oxygen interstitials, zinc substitutions, oxygen substitutions, and hydrogen substitutions[42]. Extrinsic defects are being introduced into zinc oxide to try and alter the properties of the material that are caused by the intrinsic defects already present. Doping zinc oxide with nitrogen is being performed to fill vacancies and introduce interstitials into the crystal lattice for example[43].

Energy Bands. Zinc oxide is a wide band gap semiconductor with a band gap energy of 3.36 electron volts (eV). The multiple types of defects in the crystal structure introduce many defect energy states between the valence band and the conduction band. These defect states alter the optical and electrical properties of the nanomaterials considerably. The intrinsic defects of the zinc oxide crystal structure lead to the n-type semiconducting nature of zinc oxide. This was believed to be due to the oxygen vacancies that are heavily prevalent in zinc oxide samples, but recent research has shown that this is not the case[44,45]. It has been found that hydrogen interstitials[46] or hydrogen substitutions[47] are likely the cause to unintentional n-type doping. Doping with another atom or molecule is being researched to try and introduce defect energy levels that may counteract or limit the intrinsic defects to alter the properties of the crystal, such as doping with nitrogen in an attempt to generate p-type doped zinc oxide[48].

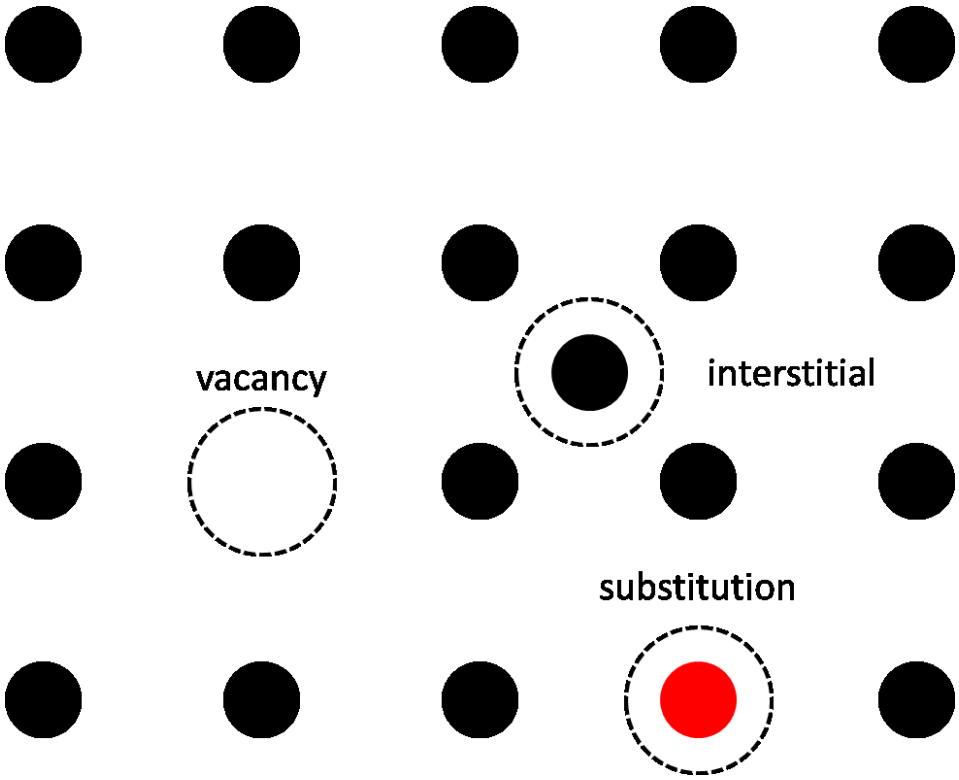

Figure 3: Three different possible point defects within crystal structures.

Figure 4 illustrates the different energy levels that exist in the zinc oxide crystal structure. The bottom band is the valence band and the top is the conduction band. The different levels in between are due to the different kinds of defects in the crystal lattice. E_g is the value of the energy band gap from the valence band to the conduction band. V_{Zn} and V_O are vacancies of zinc and oxygen atoms respectively. Zn_i and O_i are zinc and oxygen interstitial defects respectively. The O_{Zn} is an oxygen anti-site or substitution where oxygen replaces a zinc atom in the crystal lattice[49]. The arrows represent the transition of the electrons either from the conduction band or the valence band to the defect energy states. These values were calculated through density of state calulations[42] and the data does not represent all the possible defect energy levels that could be present.

There are also possible transitions not shown in the diagram, such as from one defect energy state to another defect energy state.

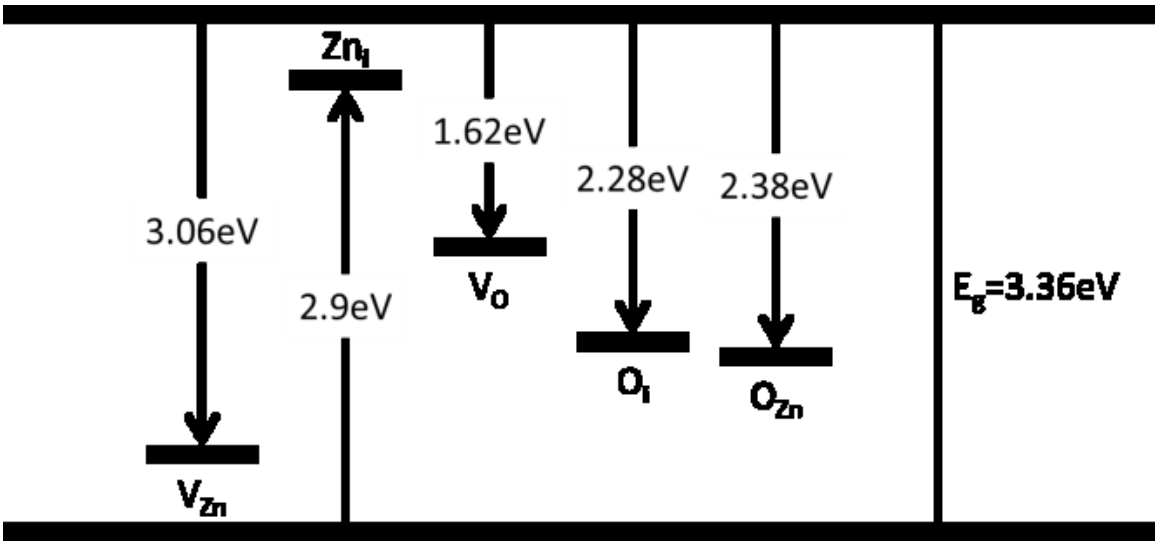

Figure 4: Intrinsic defect energy states of zinc oxide. From left to right: zinc vacancy, zinc interstitial, oxygen vacancy, oxygen interstitial, and oxygen anti-site.

Hydrothermal Synthesis

The hydrothermal synthesis is one of the many options for synthesizing nanomaterials. It's a liquid chemical approach as mentioned above and it's popular due to its simplicity and remarkable control over the structure of the nanomaterial. The one main drawback to the process is that it is a black-box synthesis technique in the sense that monitoring the growth and studying the formation of the nanomaterials is not possible. This technique is used in many different branches of science including materials science, biology, chemistry, geology and physics[50].

The process of the hydrothermal method was discovered when geologists started studying the earth's ability to generate rocks and minerals between its tectonic plates. In high temperatures and pressures, water approaches its supercritical point where its

dielectric constant decreases. In this state, water drastically increases the reaction rate and supersaturation for the particles forming around it[51].

The main variables that can alter the growth kinetics in the hydrothermal method are the precursor concentration, pH, time, and temperature, but another variable that can be used is the addition of a biomolecule into the synthesis process. Molecule assisted hydrothermal synthesis is the use of an organic molecule in the hydrothermal process to influence the growth kinetics of the nanomaterials. The interaction between the inorganic and organic species alters the size and shape of the materials[52]. Shapes such as the dumbbell and disk might not be able to form without the assistance of the molecule in the synthesis process[53]. The assistance of the biomolecule can also alter the formation of the nanomaterials in a way that can alter the properties of the material such as increasing its physical stability[54].

One possible biomolecule for use in hydrothermal synthesis is lysine[55]. Lysine is a simple biomolecule that has been shown to interact with zinc oxide nanostructures to enhance their properties. A lysine treatment has been shown to interact with zinc oxide nanowires to enhance its photoconduction in the ultraviolet region[56]. Lysine is an amino acid and freely dissoluble in water. Degradation of lysine occurs at approximately 100°C[57]. Figure 5 displays the ball and stick model of the lysine molecule.

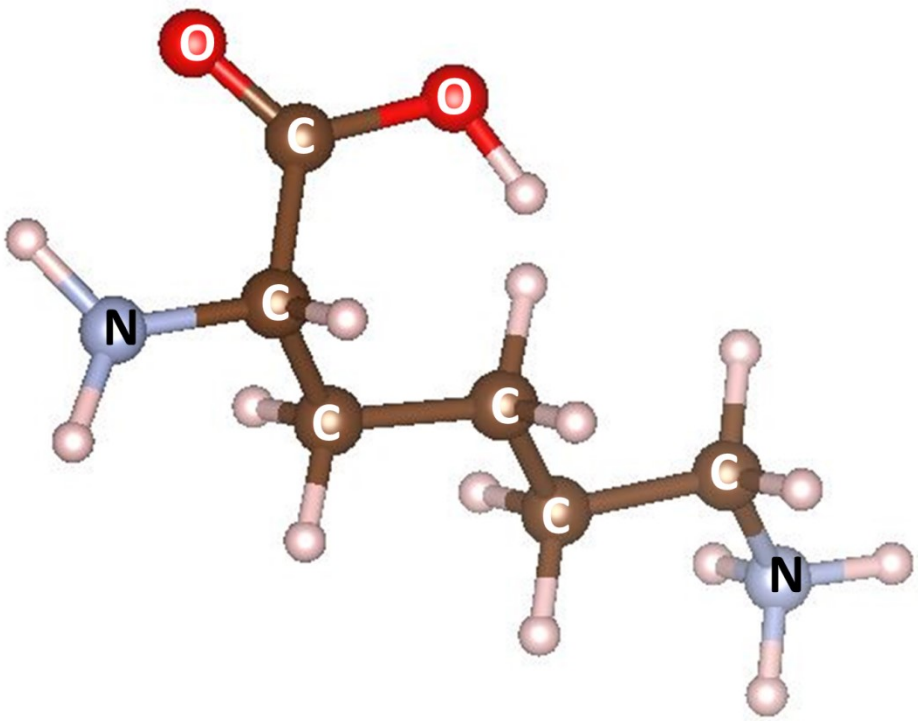

Figure 5: Ball and stick model of lysine molecule with atoms labeled.

EXPERIMENTAL

Hydrothermal Synthesis

Zinc nitrate hexahydrate ($Zn(NO_3)_2 \cdot 6H_2O$) was chosen as the precursor material and ammonium hydroxide was chosen as the reagent for the hydrothermal synthesis due to success in other research[21,58,59]. The zinc nitrate hexahydrate dissolves in water to zinc cations and other anion species and the ammonium hydroxide (NH_4OH) dissolves to ammonium cations and hydroxide anions. The full chemical reaction in the hydrothermal process is presented below[60].

$$NH_4OH \rightarrow NH_4^+ + OH^-$$

$$Zn^{2+} + 4NH_4OH \rightarrow [Zn(NH_3)_4]^{2+} + 4H_2O$$

$$Zn^{2+} + 2OH^- \rightarrow Zn(OH)_2$$

$$2OH^- + Zn^{2+} \rightarrow ZnO(s) + H_2O$$

The hydrothermal process, as previously mentioned, is dependent on the environment of the growth process. The environment is described mainly as the time and temperature of growth, the pH of the system, and the concentration of precursor material. Another variable is the introduction of a biomolecule into the system. L-lysine is a simple amino acid that has been shown to interact with zinc oxide materials and alter the properties of the material[56]. In this study, the hydrothermal process was altered to study the effects of the addition of L-lysine to the system and the temperature during growth. Six different samples were made with varied temperatures and half with and half without L-lysine added before the synthesis process.

The precursor solutes are measured out and then dissolved in 20 mL of deionized water (DI). The molarity was set at 0.15 M which is 0.9 grams of zinc nitrate hexahydrate for the precursor material. 0.2 grams of L-lysine was used as a treatment molecule for the synthesis process and was added to half of the samples grown. The initial solution is sonicated for 10 minutes to completely dissolve the materials into the deionized water.

The initial pH of the solution is measured using a Milwaukee MW 102 pH/Temp Meter. The pH meter is calibrated before each use to ensure accuracy in the readings. Addition of sodium hydroxide is used to alter the pH of the initial solution to a pH value of approximately 9 which has been found to form nanorods with the parameters we are using[21]. The sodium hydroxide is measured using a micropipette and after each addition of sodium hydroxide, the solution is sonicated for five minutes before the pH is tested and altered again.

When the pH reaches 9, the solution is transferred into a Teflon liner. The lid to the liner is sealed using Teflon tape before the liner is placed into a metal jacket. This is used to prevent any of the water vapor from escaping during heating. The entire metal enclave set-up is placed into the furnace and heated for 6 hours at the desired temperature.

When the bake is done, the solution in the Teflon liner appears as a clear liquid with a solid precipitate at the bottom of the liner. The solution is mixed using pipettes before being transferred to centrifuge tubes. The solutions are then centrifuged for ten minutes. The excess water is drawn out using a pipette and new deionized water is put into the tube. The solution is mixed using a pipette before centrifuging again for 10

minutes. This process is done three times with DI water and three times with methanol. This helps to remove any excess non reacted solute present after the bake.

The solution is mixed with deionized water once more and transferred to a crucible using a pipette. The crucible is baked in the oven at 90°C for an hour to evaporate any water from the material. The nanopowder is then finally removed from the crucible with a spatula and stored in vials. The complete parameters for the samples are listed in Table 1 below.

Table 1: Experimental parameters for hydrothermally grown zinc oxide nanomaterials

Temperature (°C)	Lysine addition	Molarity (M)	$Zn(NO_3)_2$.6H2O (g)	L-lysine (g)	DI (mL)	pH
70	No	0.15	0.9	0.0	20	10
70	Yes	0.15	0.9	0.2	20	9
85	No	0.15	0.9	0.0	20	9.5
85	Yes	0.15	0.9	0.2	20	9
200	No	0.15	0.9	0.0	20	10
200	Yes	0.15	0.9	0.2	20	10

Scanning Electron Microscopy and Energy Dispersive X-ray Spectroscopy

The scanning electron microscope (SEM) is a powerful non-invasive instrument for viewing samples at the nanometer scale. This allows for information about the size and shape of the material to be determined. An energy dispersive x-ray spectroscopy

(EDX) detector is typically used in the same system for spot specific elemental analysis of the sample.

Figure 6 displays a cross section of the scanning electron microscope. The main components of the SEM are the electron gun, lenses, apertures, EDX detector, and the back-scatter detector. The electron gun creates a beam of high energy electrons that are focused using electromagnetic coils called lenses and filtered using physical apertures. The beam is rastered along the sample from left to right and top to bottom by varying the electromagnetic field in the scanning coils and the backscatter detector measures the intensity of the electrons scattered from each pixel spot. This measurement is converted to gray scale and creates an image.

These high energy electrons have a probability of interacting with electrons bound to the nucleus of the sample and can eject them from the atom. Electrons in higher energy levels will transition to the lower energy level and emit an x-ray with energy equal to the change in energy between the electron orbitals. These transition level energies are characteristic of the type of atom and by measuring the energy of the x-ray using the EDX detector, elemental composition can be determined.

The SEM at Missouri State University is the FEI Quanta 250 Scanning Electron Microscope. The microscope was operated using a 20 kV accelerating voltage, a working distance of 10 mm, a spot size of 3.0, and an aperture value of 6. These values are fairly standard for viewing nanomaterials as it limits the aberrations for that particular size regime. The EDX was set to a 3 minute accruement time for good statistical elemental composition determination in a rectangular area of the sample. The EDX was performed

on several different areas of the sample to get a good statistical average of the elemental composition.

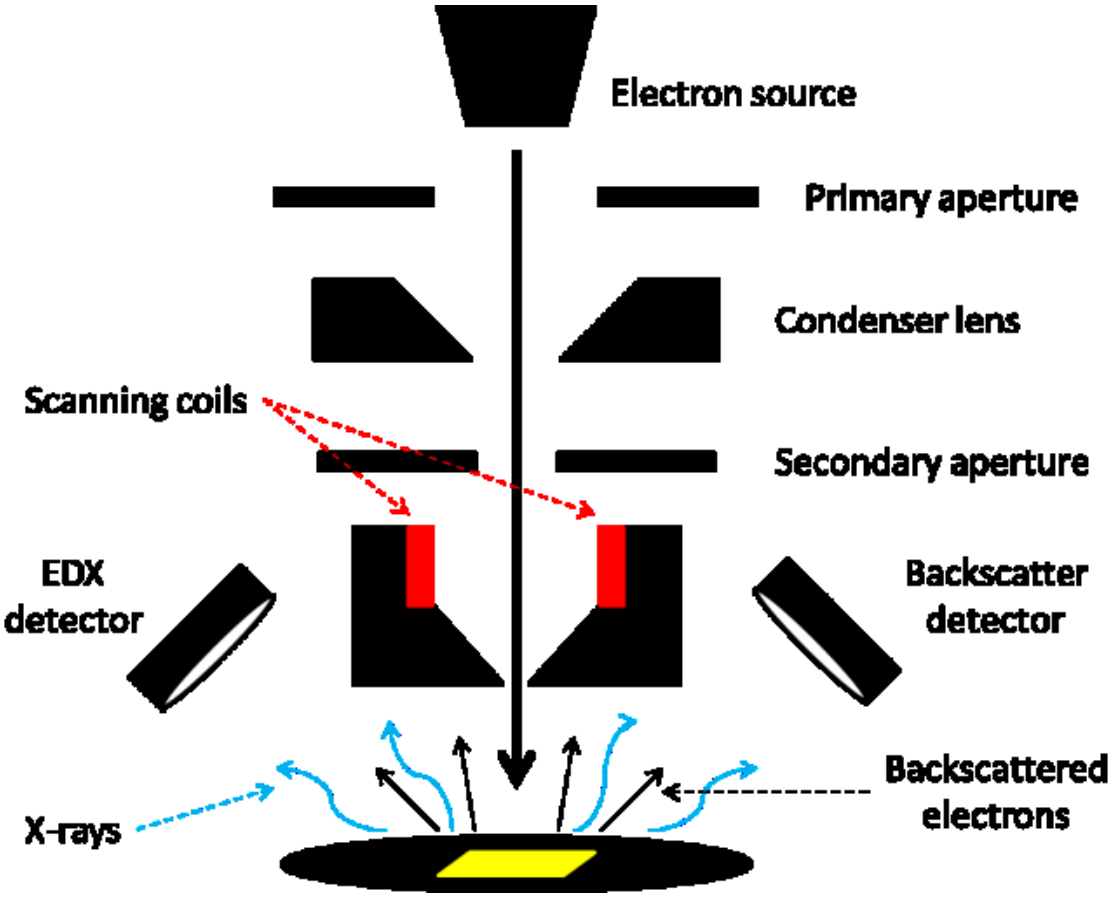

Figure 6: Cross section of the scanning electron microscope illustrating the main components in the operation.

The zinc oxide powders were pressed down onto two sided copper tape adhered to the sample holder nib and then placed into the SEM. The copper tape keeps the particles stationary during imaging and allows for conduction of the high energy electrons impinged on the sample. The electrons must be grounded away from the sample to prevent an aberration called charging where the electrons build up in the sample creating an electric field that bends the electron beam causing a distortion to the image.

X-ray Diffraction

The x-ray diffraction technique is used to study the crystal structure of materials. It is a non-invasive technique used for crystalline materials. Through analysis of the obtained spectrum, information about the type of structure, the bond length, the bond angle, and phase percentage of atoms in the material can be determined.

The main components of the x-ray diffractometer are the monochromatic x-ray source, the x-ray detector, and the sample stage which are displayed in Figure 7. The x-ray source stays stationary during measurement as it emits the x-ray beam at the sample stage. The sample stage rotates by angle θ and the x-ray detector rotates by angle 2θ. The incoming x-rays hit the sample and are scattered at angles that satisfy the Bragg condition of refraction for atomic planes in the material governed by the equation below.

$$n\lambda = 2dsin\theta$$

The n in the equation is the order which is one in the case of x-ray diffraction. λ is the wavelength of the x-ray source which is a set value for the machine. d is the atomic spacing between the crystallographic planes. θ is the scattering angle which is demonstrated in Figure 7.

The x-ray diffractometer at Missouri State University is the Bruker Discover D8 X-ray Diffractometer. The x-ray source emits at a 1.5406 angstrom wavelength using a power source of 40 kV and 40 mA. All of the zinc oxide samples were adhered to pieces of silicon by means of vacuum grease. The grease provides very little background signal and the sample is thick enough that no silicon peaks are apparent in the results. The scan parameters were 20-80 degrees at a step interval of 0.05 degrees with a 4 second acquisition time.

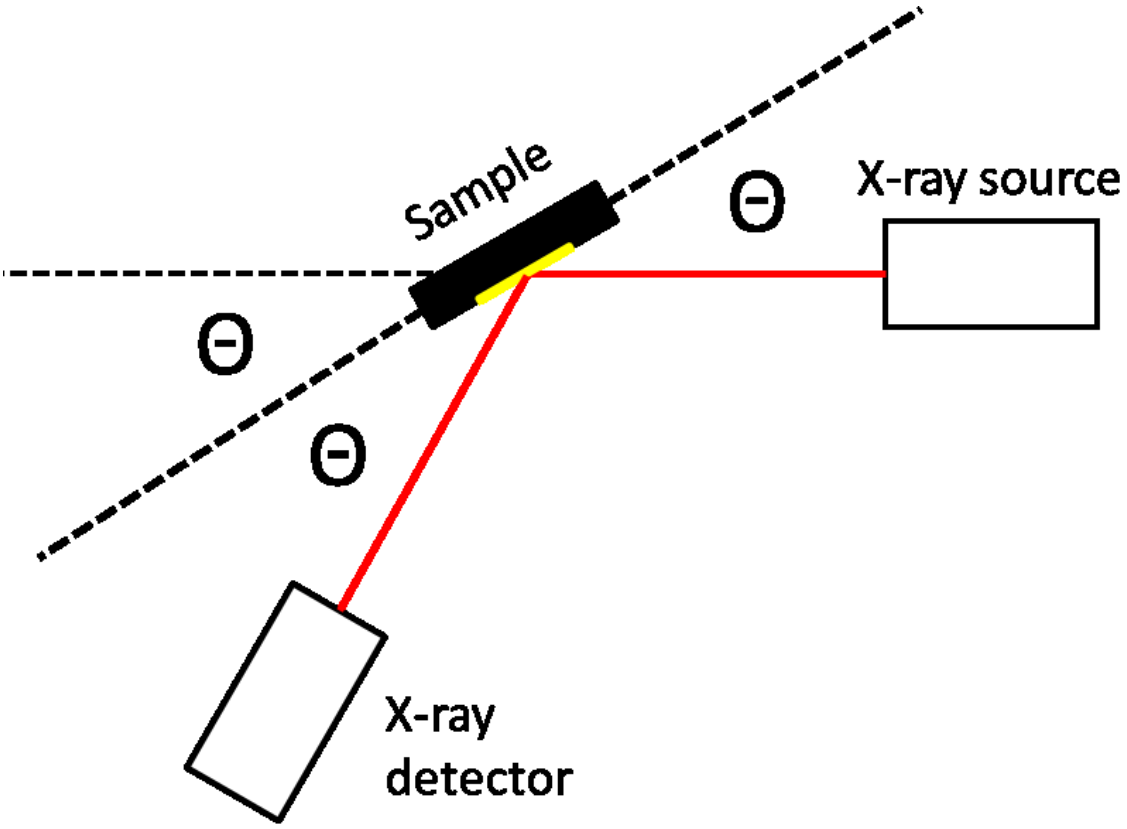

Figure 7: X-ray diffractometer diagram demonstrating the change in angle Θ of the x-ray source, sample, and x-ray detector

Ultraviolet-Visible Spectroscopy

Ultraviolet-visible (UV-Vis) spectroscopy is a technique used for measuring a material's absorption characteristics. The machine has two main components which are a white light source and a spectrophotometer. The white light source is passed through the sample using fiber optic cables and the spectrophotometer measures the intensity of light transmitted through the sample. Figure 8 displays a diagram for these main components. The intensity of light (I) passed through the sample divided by the original intensity of the white light source (I_0) is the transmittance through the sample (T). This is related to the absorption (α) of the sample by the equation below.

$$T = \frac{I}{I_0}$$

$$\alpha = -\log(T)$$

Looking at the spectra obtained from UV-Vis, it is relatively easy to notice when the energy of the photons approaches the energy of the band gap as the transmittance through the sample will decrease. A Tauc plot is an indirect measurement of the energy band gap of a material by using the spectra from UV-Vis. By plotting the absorption coefficient versus the energy of light, there is a linear regime in the graph which represents the onset of absorption of the light impinged on the sample. By extrapolating the linear region to the abscissa, it can be determined what energy of light this absorption process begins to take place and is equivalent to the energy band gap of the material.

With powder samples, a suspended solution in a liquid medium is used. 2 mg of zinc oxide nanopower was dissolved in 4 mL of deionized water to create the colloidal solutions used in the UV-Vis analysis. A quartz cuvette is used for liquid samples in the experiment. The reference spectrum for the samples is the transmittance through 4 mL of deionized water in the quartz cuvette. The quartz cuvette is approximately 5 mm long along the beam path so a large volume of the sample is exposed so that the results are not spot specific. Before testing, the samples were all sonicated for 10 minutes for complete dissolution in the deionized water. They were vigorously shaken while transporting them to the UV-Vis set-up and were tested immediately to ensure there was a uniform distribution between samples. An integration time of 250 ms was used so that the maximum of the reference spectrum was within the capability of the spectrophotometer. A boxcar width of 5 was used to smooth out the obtained spectra and 5 spectra were averaged to get a good statistical measurement.

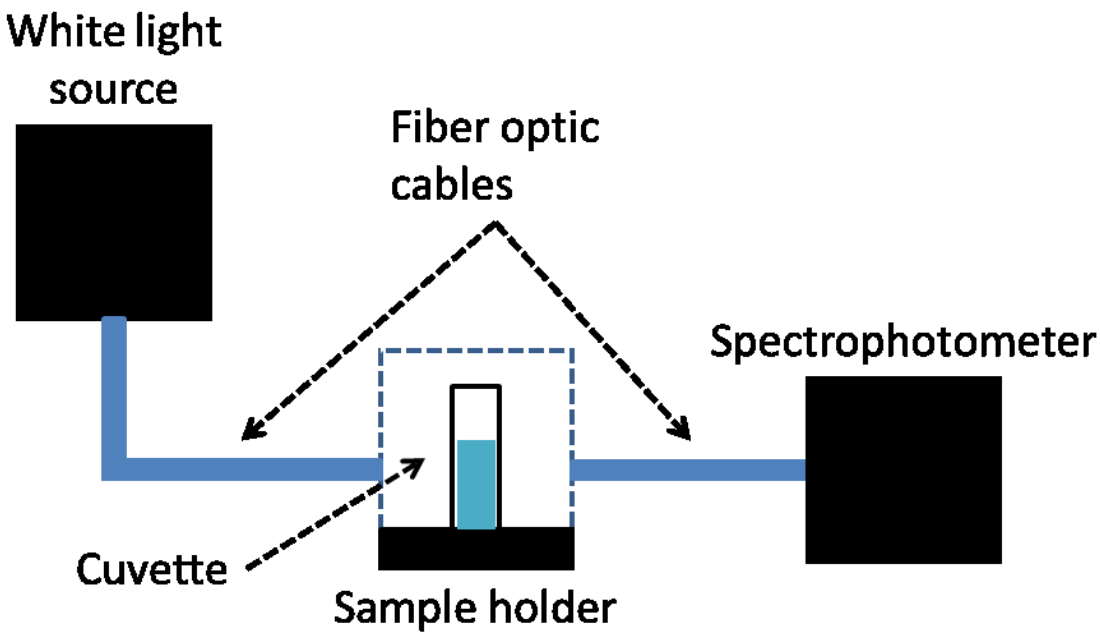

Figure 8: Ultraviolet-visible spectroscopy diagram illustrating the basic set-up for the technique.

Raman Spectroscopy

The Raman spectroscopy technique has the ability to probe information at the atomic level about the vibrational energy states present for each type of atom in the molecule or crystal. These vibrations are bond, atom, and directionally specific and can be used to identify many different features about the structure of a material. By analyzing the Raman spectrum, information about defects present in the crystal, bond force constants, and interactions between molecules can be obtained.

The principle behind the Raman effect lies in the energy bands of materials. An absorbed photon of light causes an electron to jump to a higher virtual energy state. When the electron transitions down to a lower energy level, there are three possibilities that it can transition to. It can transition down to the same energy level as it was before, which is called Raleigh scattering, or it can transition down to a lower or higher vibrational

energy level, which is called Anti-Stokes and Stokes scattering respectively. These three types of transitions are graphically illustrated in Figure 9. We choose to study the Stokes scattering as Raleigh scattering gives no information about the material and Anti-Stokes scattering occurs approximately 100x less than Stokes scattering. We can study the energy difference between vibrational energy states of the sample by taking the difference between the energy of the initial light source and the energy of the Stokes scattered light from the sample.

The Raman set-up uses a monochromatic laser as a high intensity single energy source of photons. The laser first passes through a band pass filter which eliminates stray light from passing into the system so that only photons from the laser interact with the sample. The light passes through the microscope which is used to focus the laser on one particular site in the samples being viewed. The backscattered light passes back up through the optics of the microscope and is reflected towards the edge filter. The edge filter is used to eliminate the Anti-Stokes and Raleigh scattered photons so that only the Stokes scattered photons reach the spectrophotometer. The Raman system cross section can be seen in Figure 10.

The zinc oxide samples were flattened onto a piece of tungsten carbide as it has no Raman signal and is a noiseless background sample holder. All samples were characterized using the 532 nm laser with Missouri State's Horiba Labram HR Raman-PL system. The 50x microscope objective was used to get a measurement at a highly localized spot. Multiple spots were taken to ensure sample uniformity. The scan parameters chosen was a range of 200-2000 cm^{-1}, an acquisition time of 25 seconds, and

a 15 scan average to cover all the vibrational peaks for zinc oxide and get a high intensity signal.

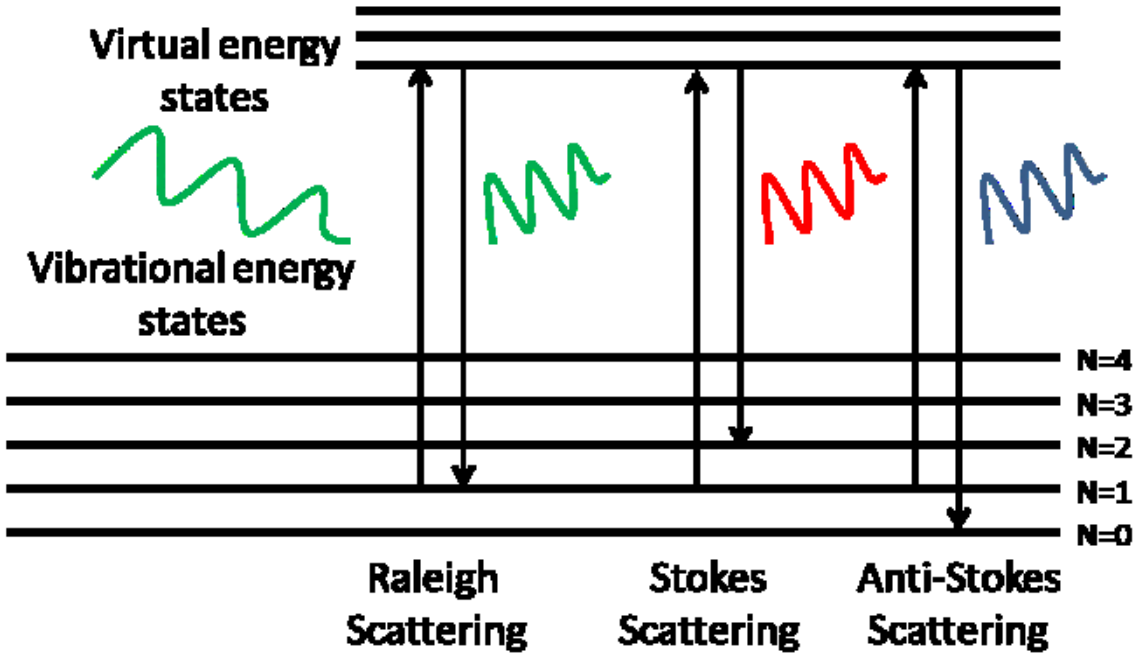

Figure 9: The Raman effect illustrated by the absorption of an incoming photon from the left causing an electron transition to higher energy state and back down again through emission of a photon to the right with energy same as (Raleigh), lower than (Stokes), or higher than (Anti-Stokes) the energy of the initial photon.

The zinc oxide samples were flattened onto a piece of tungsten carbide as it has no Raman signal and is a noiseless background sample holder. All samples were characterized using the 532 nm laser with Missouri State's Horiba Labram HR Raman-PL system. The 50x microscope objective was used to get a measurement at a highly localized spot. Multiple spots were taken to ensure sample uniformity. The scan parameters chosen was a range of 200-2000 cm^{-1}, an acquisition time of 25 seconds, and a 15 scan average to cover all the vibrational peaks for zinc oxide and get a high intensity signal.

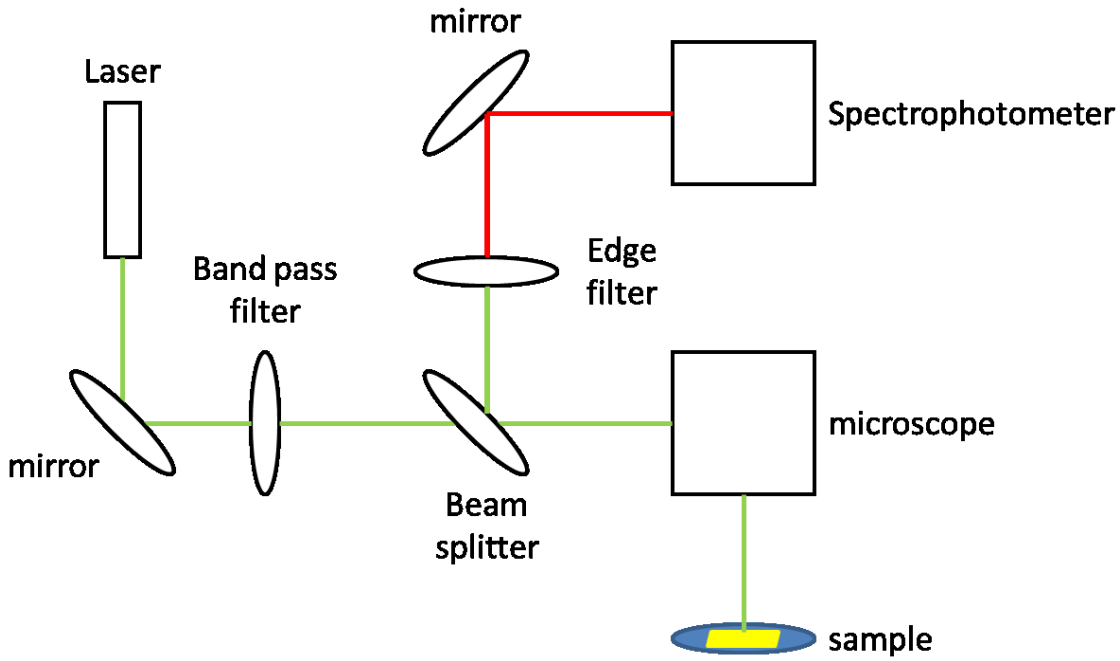

Figure 10: Raman spectroscopy cross section demonstrating the laser emission to the sample through the microscope and reflected back to the spectrophotometer through the beam splitter.

Photoluminescence Spectroscopy

Photoluminescence is another optical technique used to characterize materials that is similar to Raman spectroscopy, but with a higher energy laser. The higher energy laser has the capability to excite electrons to the conduction band instead of virtual states. These electrons will transition back to the valence band of the material by emitting a photon equal to the energy band gap of the material. There are two types of band gaps in materials. Direct band-gap materials don't require the electron to lose momentum to the crystal lattice during transitions from the valence band to the conduction band. Indirect band-gap materials require the electron to lose momentum upon the transition. These two band gaps are graphically illustrated below in Figure 11. The loss of momentum to the crystal lattice is represented by a k vector. The electron can also transition to defect states

between the conduction band and the valence band giving rise to photons emitted with energy equal to the energy of the defect states.

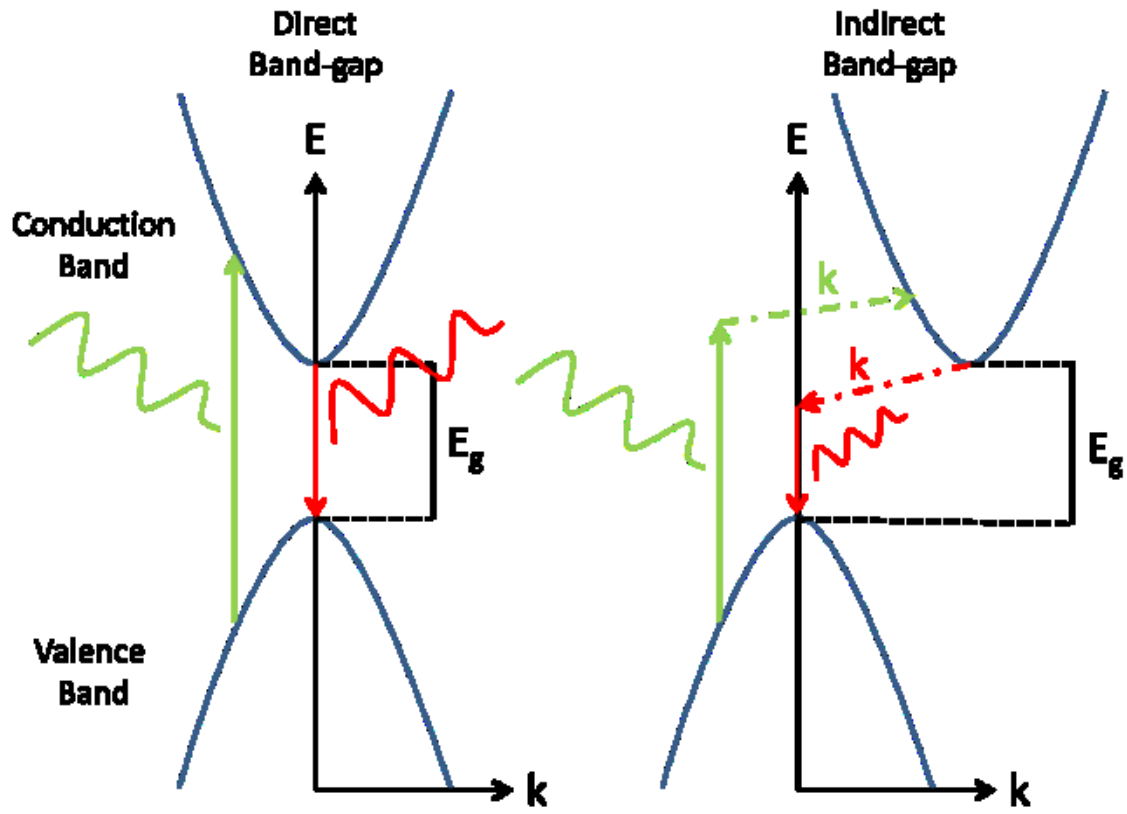

Figure 11: Direct and indirect band-gap transitions of semiconductor materials illustrating the electron jump to the conduction band through absorption of a photon and recombination to the valence band through emission of a photon.

The Raman-PL system at Missouri State has the capability for both Raman and photoluminescence measurements in the same set-up. The photoluminescence light source is a 325 nm laser. The zinc oxide samples were similarly measured on a piece of tungsten carbide to prevent any background signal. The 15x near ultraviolet microscope objective was used for localized measurements and multiple spots were taken for each sample. The scan parameters was a range of 1-3.5 eV, acquisition time of 25 seconds, and

an average of 15 scans to cover the entire band spectrum of zinc oxide and provide high intensity scans of the samples.

X-ray Photoelectron Spectroscopy

X-ray photoelectron spectroscopy (XPS) is a surface elemental characterization technique. This technique allows for the characterization of elemental composition and electronic states of atoms present on the surface of the material. Etching can be done to remove some layers from the surface to reveal bulk material underneath. The process must be done in ultra-high vacuum for accurate measurements.

Figure 12 displays a cross section of the XPS set-up. The premise behind the technique uses x-rays to excite electrons out of the material. These electrons are analyzed by an electron energy analyzer which uses a magnetic field to bend the electrons around to a detector. The energy of the x-ray photon is known and the kinetic energy of the ejected electron is measured, which means the binding energy of the electron can be determined by using the equation below.

$$E_{binding} = E_{x-ray} - E_{electron} - \phi_{spectrometer}$$

The last term is the work function of the spectrometer and is a detector specific constant. The binding energy of the electron is characteristic of the element in the sample and the number of electrons that are ejected is dependent on the amount of element present. This information allows the determination of the type of element present and the concentration of it in the sample.

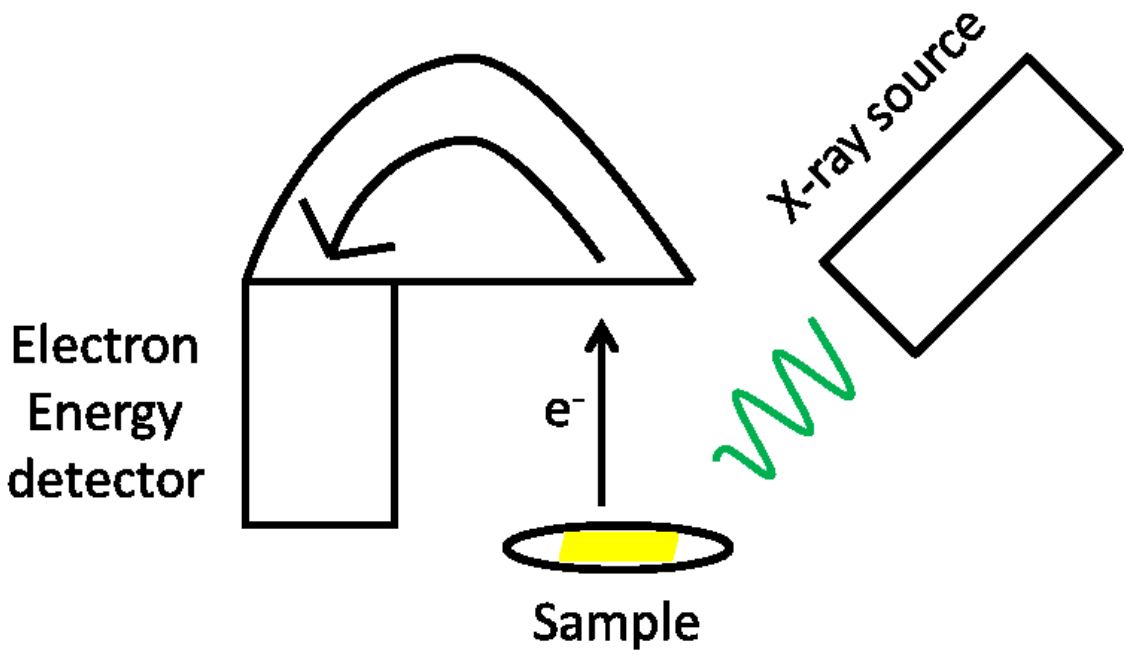

Figure 12: X-ray photoelectron spectroscopy cross section where the x-ray source ejects electrons from the sample and the electron's energy is measured through the detector.

The zinc oxide powder samples were prepared on pieces of silicon and loaded into a load-lock chamber. The load-lock chamber is pumped down over night before the samples are moved over to the ultra-high vacuum chamber for analysis. The x-ray source is an aluminum K_α emission of 1.486 keV. An overall scan from 1400 eV to 0 eV was taken with a 0.5 eV step size and a 10 scan average before sampling for specific elements was performed. The focused scans on specific elements were done with a 0.1 eV step size and a 20 scan average for high resolution results on specific elements.

RESULTS

Scanning Electron Microscopy and Energy Dispersive X-ray Spectroscopy

Images of the different samples from the scanning electron microscope are presented in Figure 13. It is clearly evident that lysine modifies the growth process of the nanomaterials during hydrothermal synthesis altering the morphology of the obtained samples. It is not a discernable uniform change between samples though.

Comparing 70°C and 85°C with and without lysine, the lysine modifies the growth process to increase the size of the nanoparticles from 50-100 nm to 500-700 nm. The petal shape of the nanoparticles remains similar though the samples with lysine have a more uniform size and shape distribution. Comparing the samples grown at 200°C though, we see that the size is again altered, though not as extreme as 70°C and 85°C, but the shape between the lysine and non-lysine samples is drastically modified. The 200°C sample with lysine has zero c-axis growth and forms nanoplatelets while 200°C without lysine formed dots and petal shape nanoparticles.

The increase in size indicates that lysine is playing a role in the growth kinetics as the zinc oxide nanostructures are forming. The lysine is altering the surface energy during growth enhancing the growth along different facets than would not normally be possible without the addition of lysine. The morphology changes as the temperature is increased to 200°C as the lysine molecule breaks down at 100°C. The constituent parts of lysine again alter the growth kinetics of the nanomaterials to form platelets instead of petal shapes.

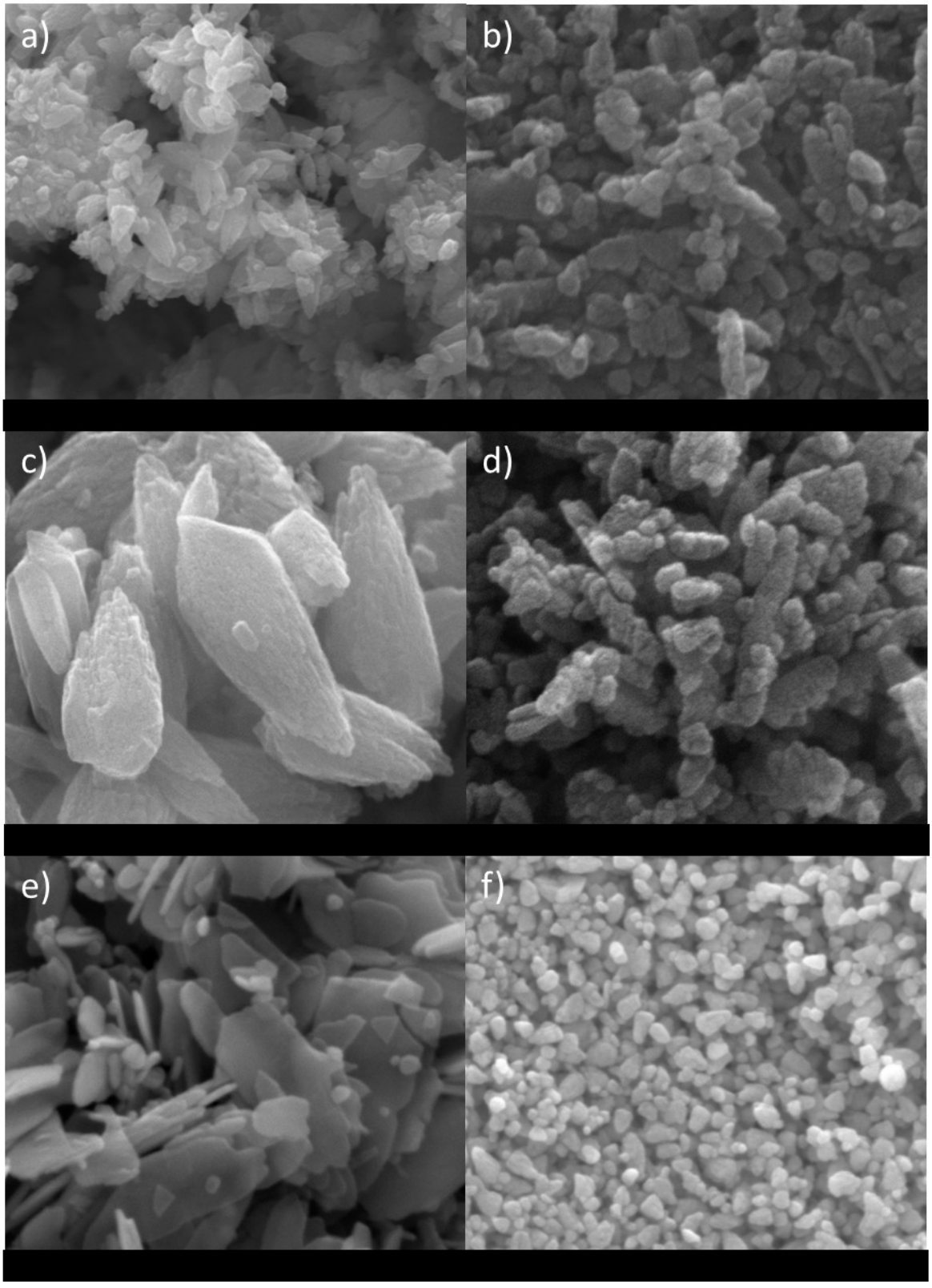

Figure 13: SEM images of ZnO nanoparticles grown at 70°C with a) lysine and b) no lysine, 85°C with c) lysine and d) no lysine, and 200°C with e) lysine and f) no lysine.

Energy dispersive spectroscopy was done in the same setting as the scanning electron microscopy. Regions scanned are approximately$1\mu m^2$. Figure 14 gives an example of an EDX scan in one area. The left hand side image is the SEM image with a square where the x-ray readings are being recorded. The right hand image is the spectrum of x-ray energies being received by the detector. Oxygen emits x-rays at 0.52 keV and zinc emits x-rays at 1.01 keV which is indicated by the Zn and O balloons in the spectrum. No other elements were detected in the scans other than zinc and oxygen.

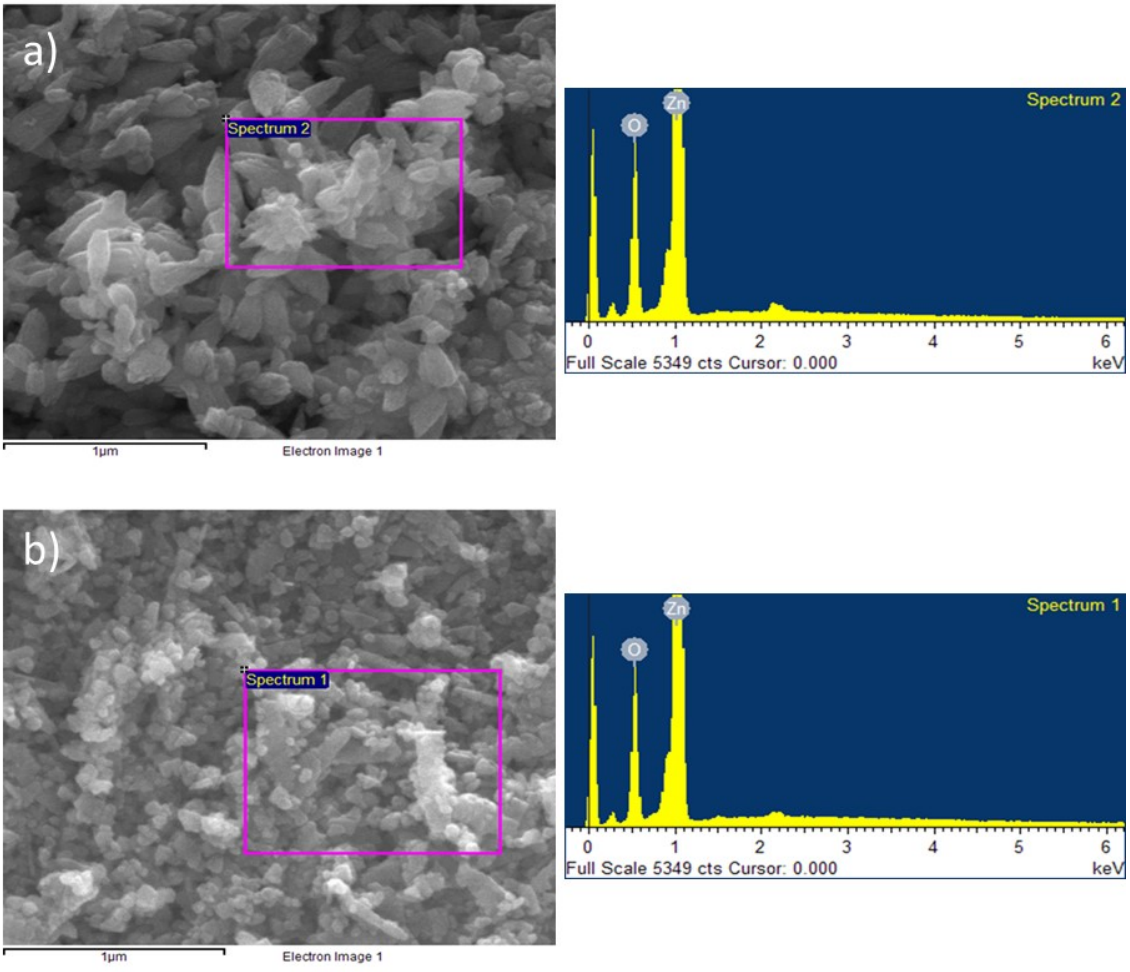

Figure 14: Energy dispersive x-ray spectroscopy results for zinc oxide nanoparticles grown at 70°C a) with lysine and b) without lysine.

The EDX spectrum is analyzed by the INCA software that runs the EDX detector and determines the atomic percentage of the elements present in the scanned area. Multiple spots were taken to get an average over the sample for elemental composition. The results from multiple scans for each of the samples are displayed in Figure 15. The EDX measurement is only a surface analysis technique and can't give information about the bulk of the material. The values presented give some insight into the surface composition though the values cannot be exact as the values are unreasonable for atomic percentages. The results indicate that samples grown with lysine have a higher percentage of oxygen atoms than zinc atoms for the three temperature values. This could be due to the particular facet that is emphasized by the petal shape as the facet could have more oxygen exposed than zinc.

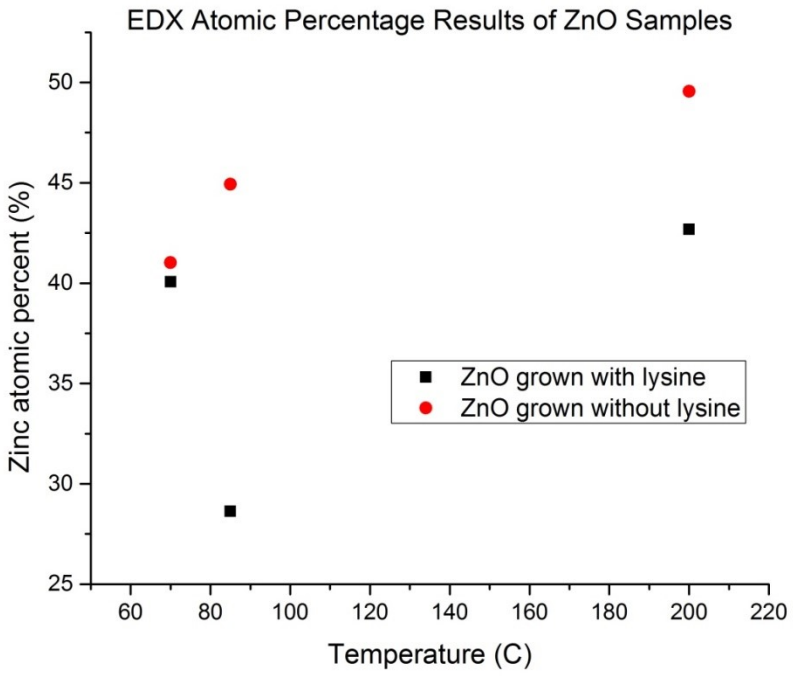

Figure 15: Energy dispersive x-ray spectroscopy atomic percentage results for each temperature growth and separated by color for samples grown with and without lysine.

X-ray Diffraction

X-ray diffraction results are displayed in Figure 16. There are no apparent abnormalities between the different sample temperatures or between samples with and without lysine. All the peaks corresponding to the zinc oxide hexagonal wurtzite structure are apparent in each of the scans. The miller indices are displayed in the figure corresponding to all the different planes in the crystal structure[61].

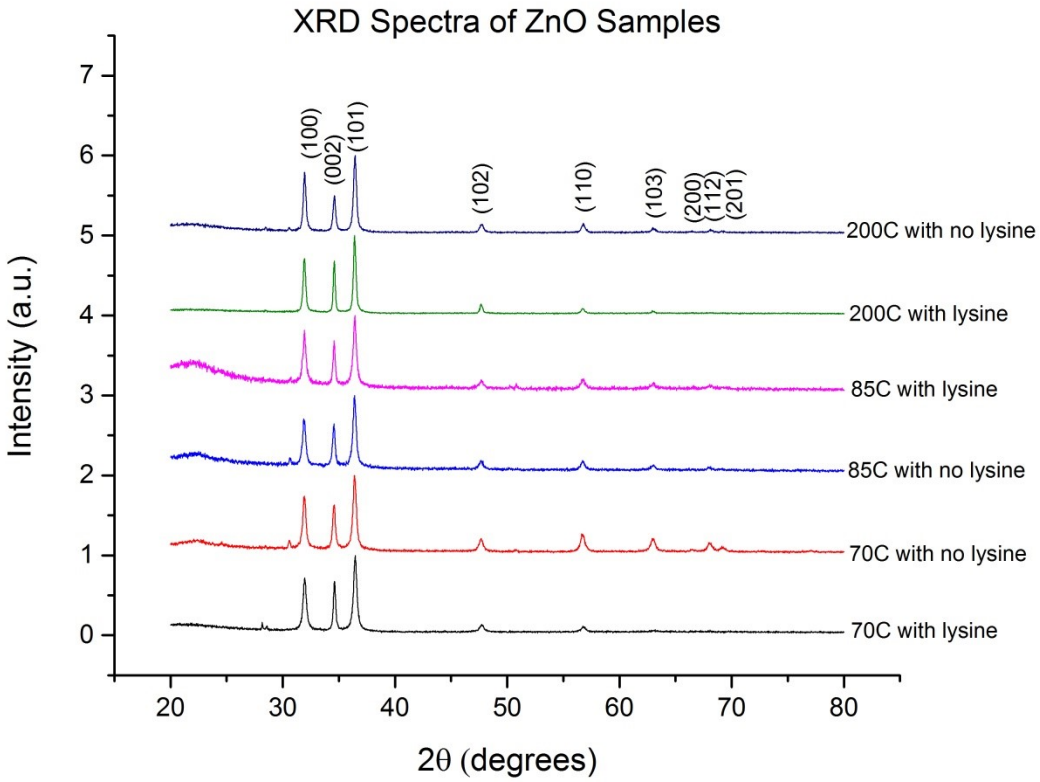

Figure 16: X-ray diffraction spectra for each sample staggered for comparison with the miller indices for the atomic planes listed above the corresponding peaks.

Topas crystallography software was used in fitting the scan data to the zinc oxide standard crystal information files (.cif) to determine any minute changes in the crystal

structure. All of the scans matched up with the standard zinc oxide crystal structure obtained from the Open Crystallography Database. In Figure 17, the results from each of the fittings can be seen. The black line is the original spectrum, the red line is the calculated spectrum including a background on the order of 5, the pink line is the calculated spectrum without the background, and the blue line is the difference between the calculated spectrum and the original. All of the scans were fit to a goodness of fit value of 1.20 or lower. The atomic occupancy was the last parameter to be fitted so that the fitting was first performed to the structure and lastly to the atomic occupancy. The absence of any contamination peaks indicates that the sample is purely zinc oxide hexagonal wurtzite structure. Any contamination that may or may not be in the sample must be amorphous.

From the fitting, information about the crystal lattice parameters and atomic occupancy can be determined. The lattice parameters for the different samples change only minutely between each temperature and with or without lysine. The c/a ratio remains largely unaffected as it stays close to the standard value of 1.6. The zinc and oxygen occupancy deviate from the stoichiometric 1:1 ratio. Figure 18 graphically illustrates the results for the atomic occupancy in the samples. The up arrows represent the zinc and the down arrows represent the oxygen occupancy and the blue arrows are growth with lysine samples while the red arrows are without. At 70°C, the sample with lysine has a greater amount of zinc than oxygen and vice versa for the sample without lysine. At 200°C, the opposite is present as the sample with lysine has a greater amount of oxygen than zinc and vice versa for the sample without lysine. At 85°C, both samples have a close 1:1 stoichiometric amount of zinc to oxygen atomic occupancy.

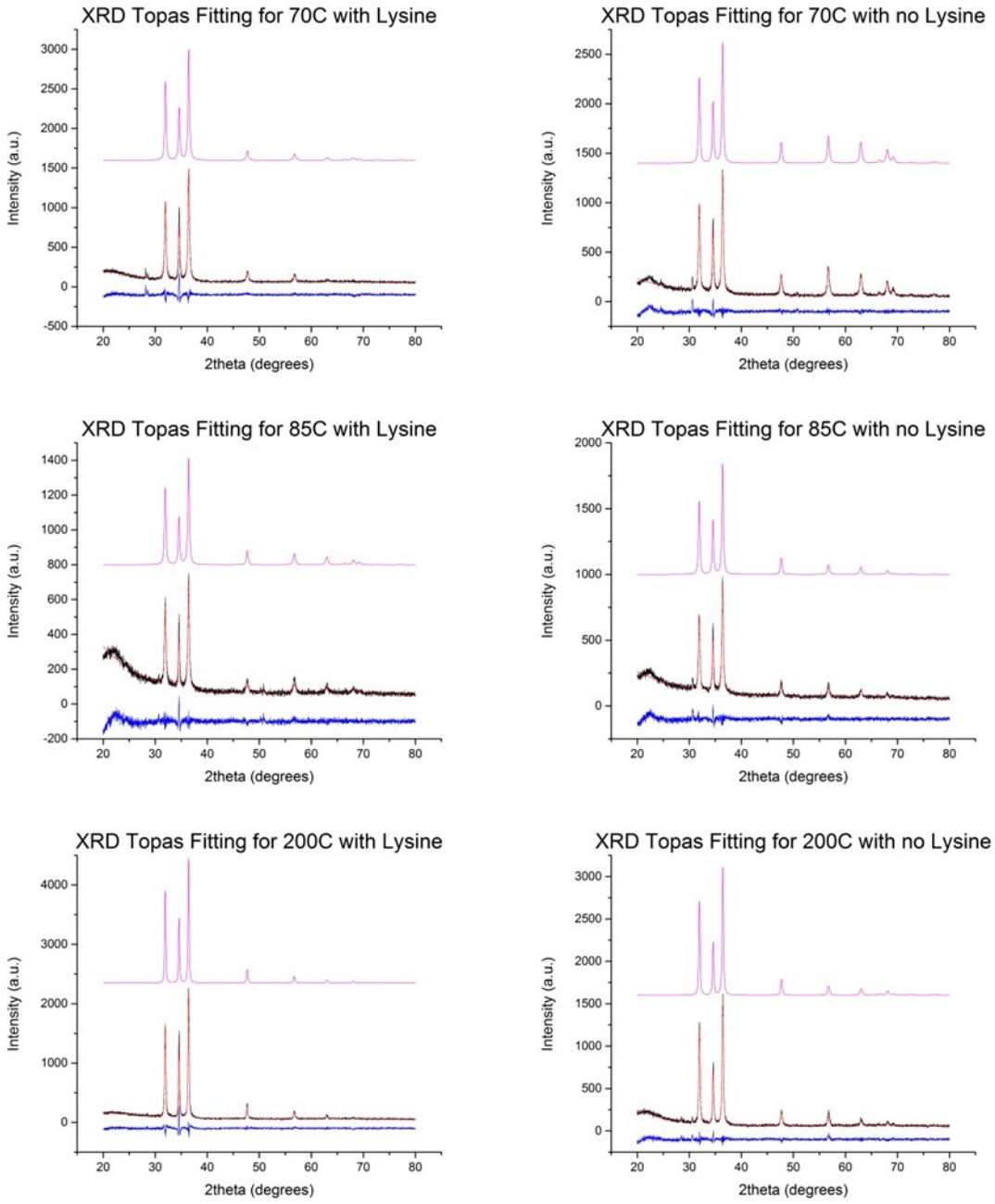

Figure 17: Topas crystallography fitting results for x-ray diffraction spectra. The black lines represent the original spectrum data, the red lines represent the fitted analysis including a background of the order of 5, the pink lines represent the fitted analysis without the background, and the blue lines represent the difference between the calculated fitted analysis and the original data.

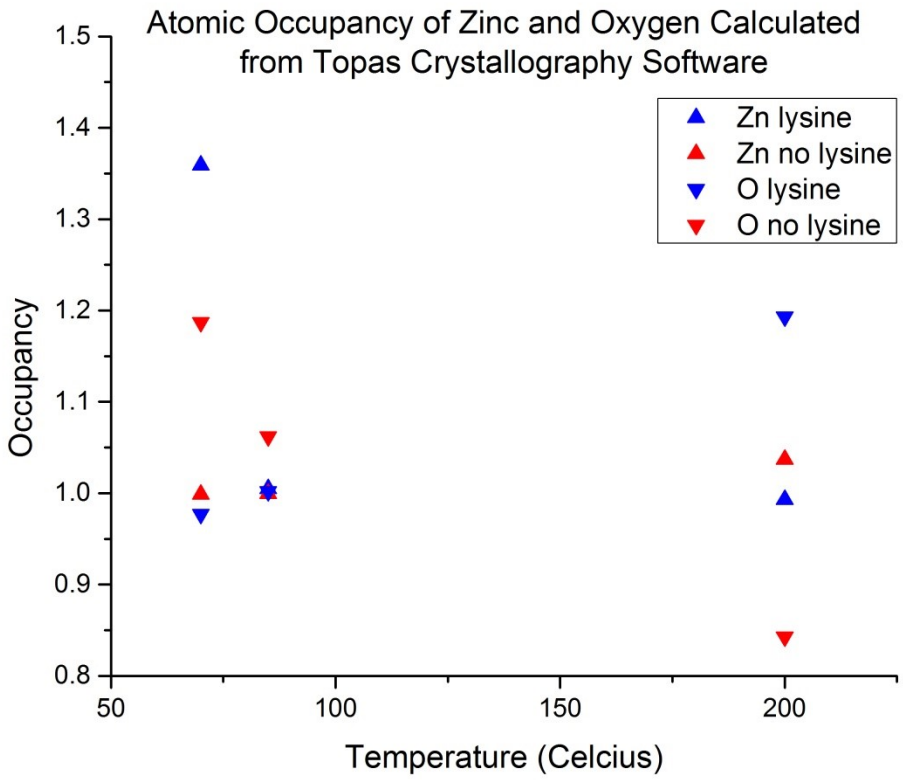

Figure 18: Atomic occupancy results from Topas crystallography analysis of x-ray diffraction spectra. Up arrows represent zinc and down arrows represent oxygen. The blue icons represent samples with lysine and the red icons represent samples without.

Ultraviolet-Visible Spectroscopy

Ultraviolet-visible spectroscopy results clearly show a large difference between samples with and without the addition of lysine during the synthesis process in Figure 19. The samples grown at 70°C, 85°C, and 200°C are represented by the color red, green, and blue respectively. The solid lines represent samples without the addition of lysine while the dotted lines represent samples grown with the addition of lysine. The samples with lysine clearly absorb considerably greater light than the samples without lysine. It is slightly evident from the spectra that the samples with lysine absorb light at a slightly

lower energy than the samples without lysine, but more apparent when reviewing the absorption coefficient.

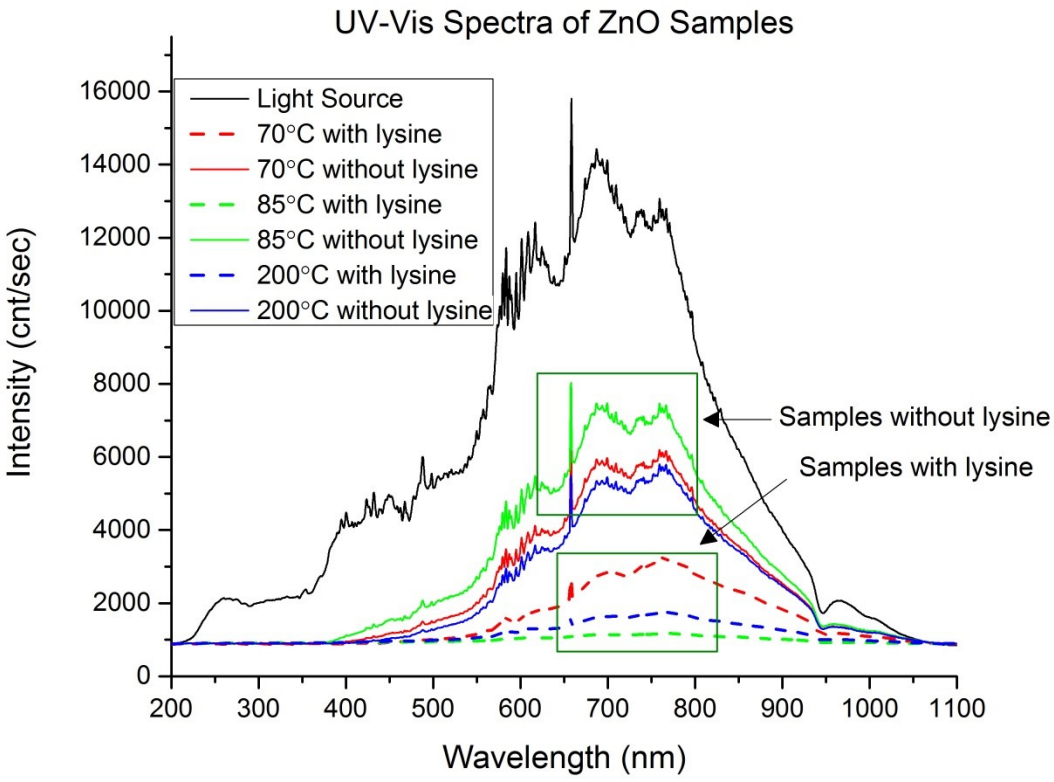

Figure 19: Ultraviolet-visible spectroscopy spectra for all samples. The growth temperature of the red color is 70°C, the green color 85°C, and the blue color 200°C. The solid lines represent samples without lysine while dotted lines represent samples with lysine.

The absorption coefficient is calculated for each of the samples and the Tauc plots are generated to determine the onset of absorption and calculate the band gap of the sample. All of the Tauc plots can be seen in Figure 20. Looking at the linear regions in the plot and extrapolating to the abscissa, the energy gap of the materials can be determined. The portion of the graph that is highlighted is the linear region corresponding

to the energy gap of the nanomaterial. Figure 21 displays the calculated band-gap values for each of the samples. The samples grown at 70°C and 85°C with lysine have a lower band gap value which explains their increased absorption compared to the samples without lysine. The samples grown at 200°C have the same band-gap, but the sample with lysine still absorbs a greater amount of light.

By comparing the Tauc plots of the lysine samples to the non-lysine samples in Figure 20, we can see that the initial increase in absorption coefficient in the lower energy regime is very different between the two at each temperature. This regime is dominated by defect energy state absorptions. Without lysine, the absorption coefficient is a much sharper incline at a higher energy value meaning there is a lower concentration of defects or defect energy states in the sample. All the samples with lysine have a greater ability to absorb light at lower energies representing an increased concentration of defects or defect energy states. The samples grown at 85°C and 200°C with lysine display an almost linear regime in the low energy absorption coefficient giving rise to their enhanced ability to absorb light.

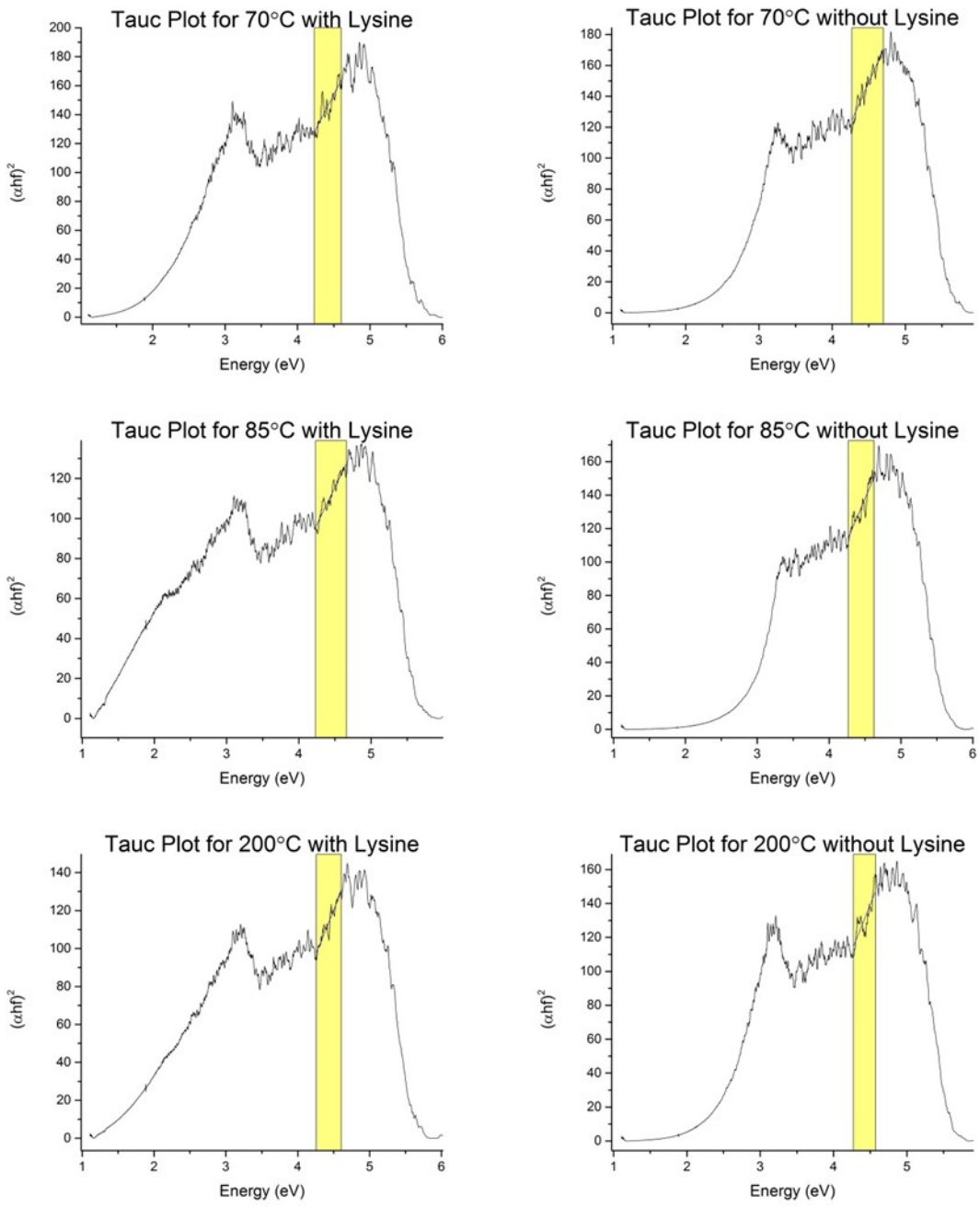

Figure 20: Tauc plots for all zinc oxide samples with highlighted regions where the linear fitting was performed to extrapolate the energy band gap.

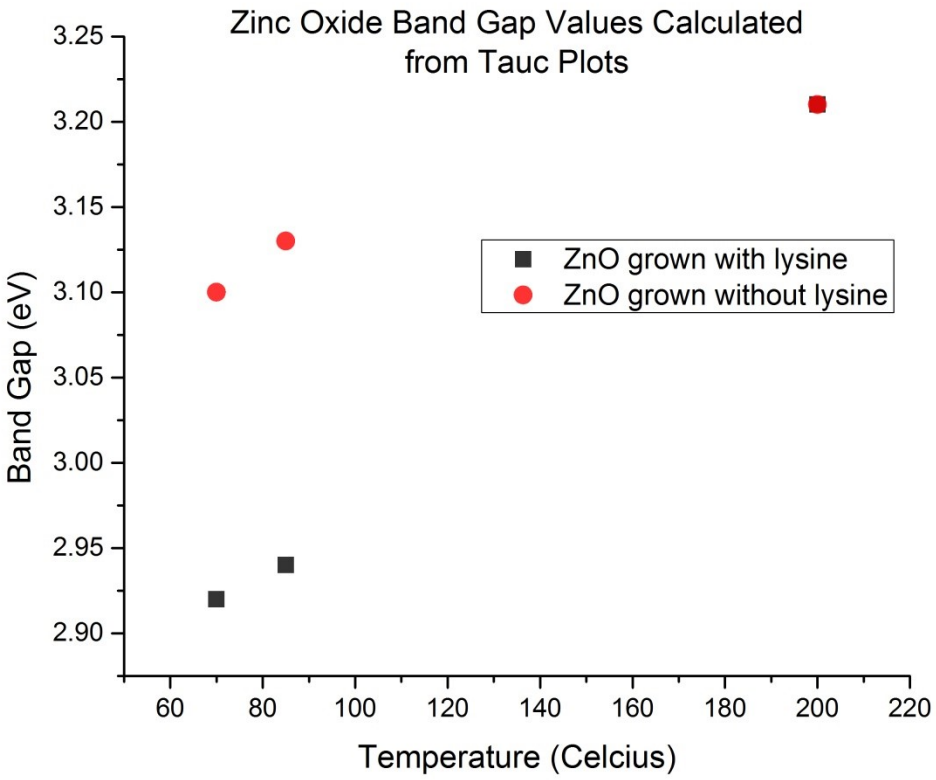

Figure 21: Calculated band gap values for zinc oxide nanomaterials using Tauc plots grown with lysine, represented by black, and without lysine, represented by red.

It can be seen then that the samples grown with lysine display a significantly greater ability to absorb light due to two reasons. The band gap of the material was decreased allowing for lower energy absorptions. The concentration of defects or defect energy states was also increased allowing for a greater absorption in the lower energy regime. The sample grown at 70°C with lysine displays a lower energy band gap, but not a greatly increased concentration of defect energy states so its absorption capability is increased, but not as much as the two samples grown at 85°C and 200°C. The sample grown at 200°C with lysine does not have a lowered energy band gap, but does have a higher concentration of defects or defect energy states and experiences an increased

ability to absorb light, but the sample grown at 85°C has the greatest enhancement. The lowered energy band-gap value and increased concentration of defects or defect energy states gives the sample grown at 85°C with lysine the most significant enhancement in absorption.

Raman Spectroscopy

The results from Raman spectroscopy gives us information on how the lattice vibrational states are changing. Figure 22 compares the Raman spectra for each growth temperature. The characteristic Raman peaks for zinc oxide are between 250 and 625 cm^{-1}. The convolution of peaks between 1000 and 1250 cm^{-1} are due to defects, mainly zinc hydroxide. Other broad peaks in some of spectra are due to background subtraction aberrations and are not part of the sample.

Figure 23 displays deconvolutions of the characteristic Raman peaks for zinc oxide. The first graph labels the different vibrations present in the convolution. The A_1, E_1, and E_2 vibrations are discussed earlier in the introduction and the 2-E_2 and 2-LA peaks are second order Raman scatterings. The most obvious difference between the samples with and without lysine is the presence of the A_1(TO) mode of vibration. The lysine sample's deconvolutions would not converge without the inclusion of the peak and attempting to include the peak in the samples without lysine lead to a zero intensity peak. The addition of lysine in the growth process has modified the nanostructure to enhance the presence of this c-axis vibrational state.

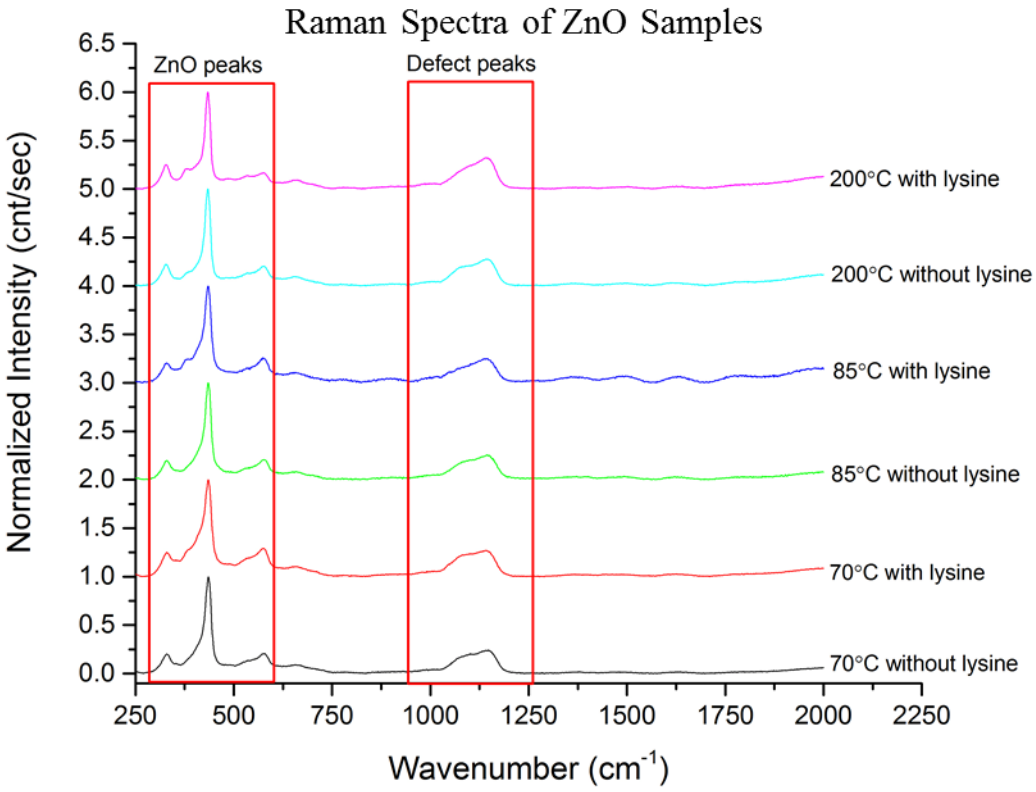

Figure 22: Raman spectra of zinc oxide samples staggered on a normalized intensity graph with the growth parameters listed on the right side. The characteristic ZnO Raman peaks and ZnO defects peaks are boxed.

Analysis on these different convoluted peaks has been done in Figure 24. The peak center and full width half max for each of the peaks has been plotted versus the temperature during the synthesis process. The red dots represent the samples without the addition of lysine and the black dots represent the samples that included lysine. Some relatively small, but noticeable trends exist within the analysis.

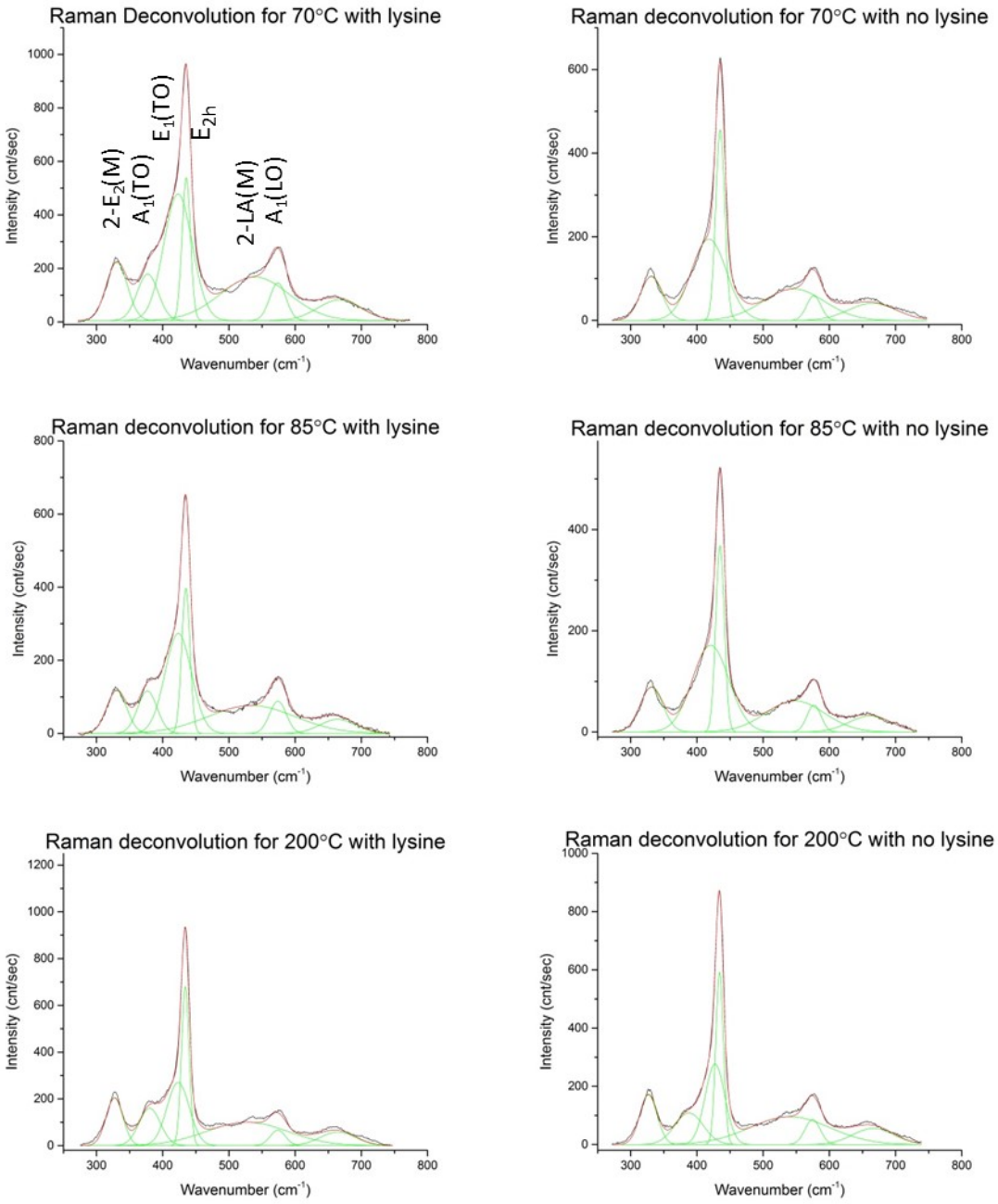

Figure 23: Deconvolution of characteristic zinc oxide modes of vibration in the Raman spectra.

The E_1(TO) mode seems to be unaffected by temperature when lysine is present during synthesis while the sample without lysine is stiffened with increasing temperature. For both of the samples though, the full width half max decreased with increasing

temperature. For both of the samples, with and without lysine, the E_{2h} vibrational mode drops to lower wavenumbers with increasing temperature. This vibrational mode involves only the oxygen atoms in the crystal. The A_1(LO) vibrational mode is generally at lower wavenumbers for the samples with lysine by 2 to 3 wavenumbers.

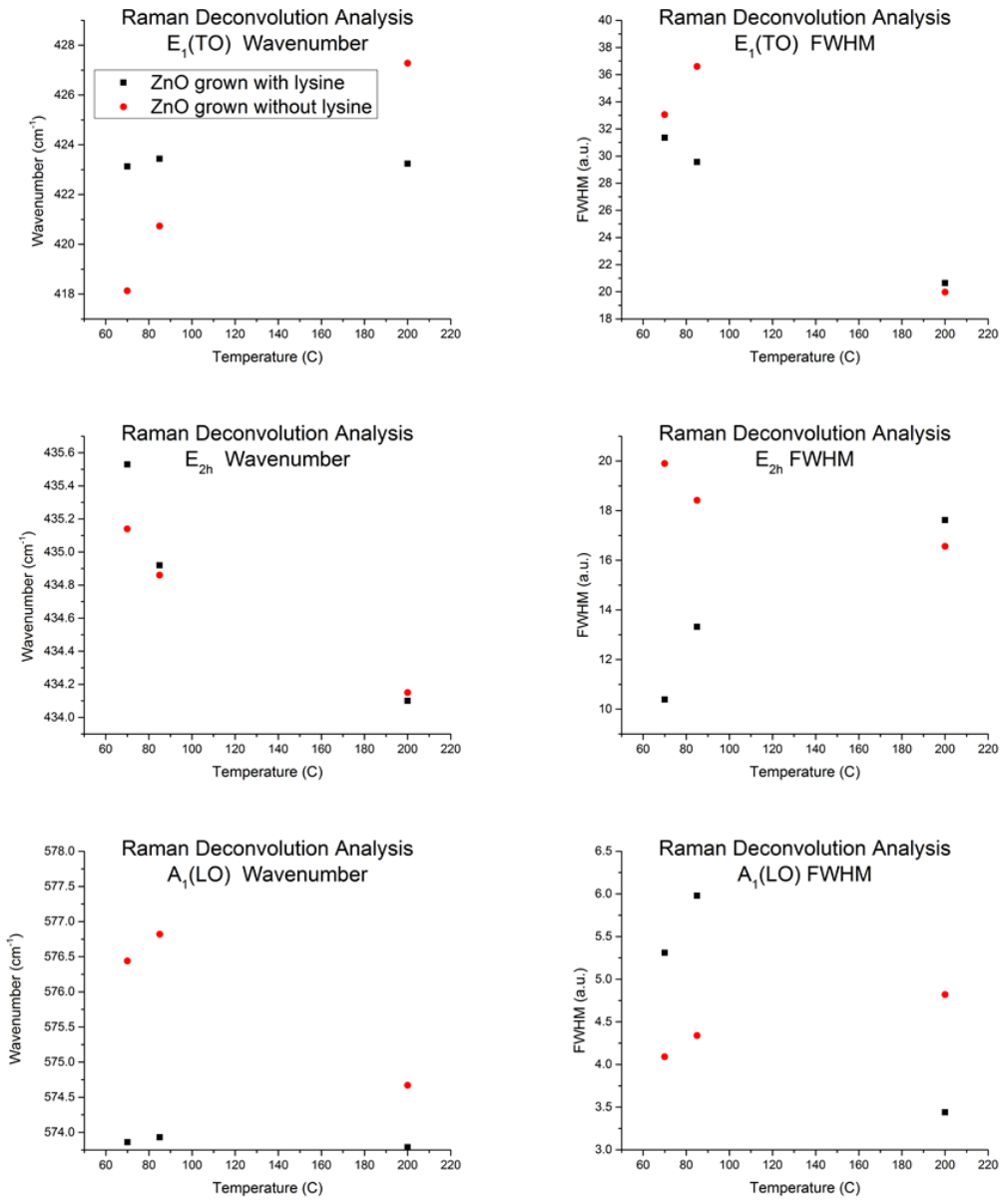

Figure 24: Analysis of the convoluted peaks from the Raman spectra where the black markers represent samples grown with lysine and red markers without lysine.

Photoluminescence Spectroscopy

Photoluminescence of the samples did not show any drastic changes and can be viewed in Figure 25. The energy band gap of zinc oxide around 3.2 eV is completely dwarfed in comparison to the defect peaks between 1.5 and 2.5 eV though all samples displayed a peak around 3.2 eV. All the samples have about the sample signature in photoluminescence. The only main difference is that the samples grown with lysine all have a slight shoulder in the defect region at lower energy. This small shoulder is due to a particular convoluted peak or peaks intensity increasing. It is indiscernible what peak or peaks are contributing to this shoulder, but this is due to a particular defect or defects being increased in concentration. Most oxygen defects reside in this energy region, but it cannot be determined for sure that this is due to an increased concentration of oxygen defects. For the samples grown at 200°C, the energy band gap of 3.2 eV is prominent enough to be detected, along with its half value around 1.6 eV. It is inconclusive why it's present at 200°C, but not at the other growth temperatures.

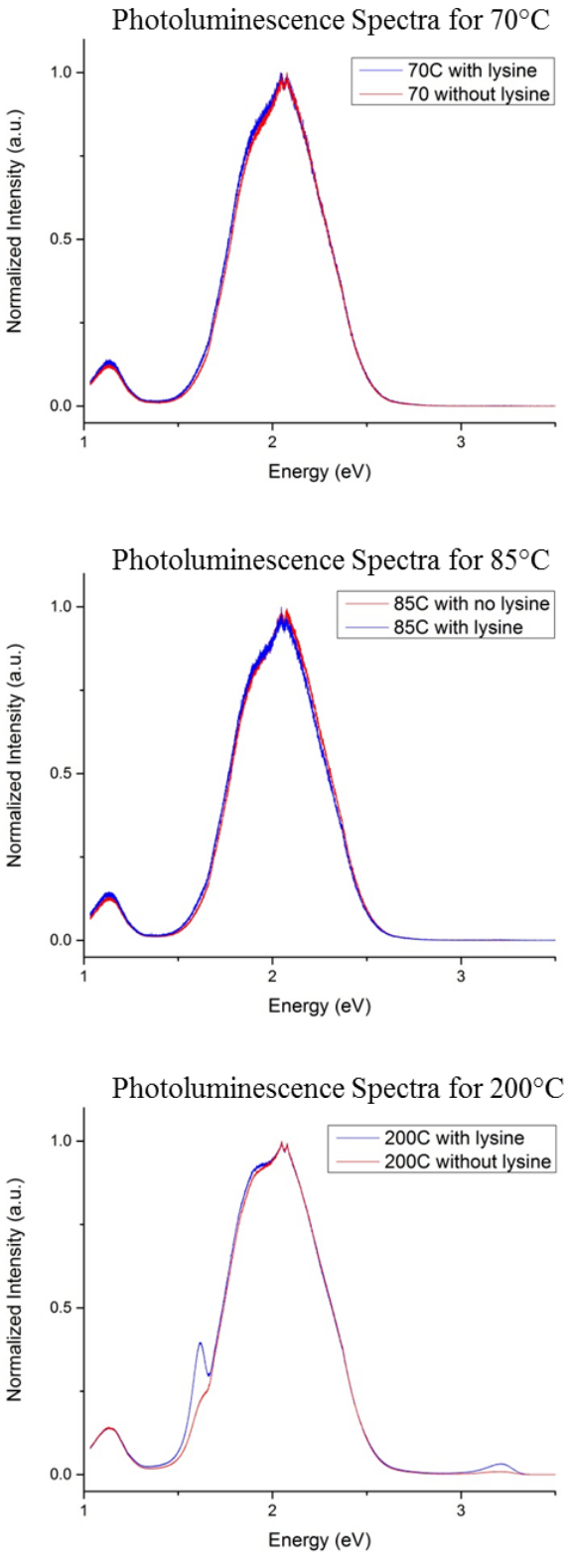

Figure 25: Photoluminescense of zinc oxide samples where blue represents samples with lysine and red represents samples without lysine

X-ray Photoelectron Spectroscopy

XPS gives us a little more information about the surface structure similar to EDX, but with a slightly greater reliability. An overall spectrum was taken to determine if there were any impurities in the samples. The elements that were scanned for high resolution were zinc, oxygen, carbon, and nitrogen. The carbon was scanned to have a good reference spectrum for normalization and the nitrogen was scanned to determine if any of the lysine molecules were still present in the sample.

Figure 26 displays one example of a full energy XPS scan analyzed in CASA XPS analysis software. The different peaks are correlated to particular elements and their electronic structure. The lines that are present are indicating peaks belonging to zinc and oxygen. The few other peaks are contamination believed to be due to the chamber. The software analyzes the area under the peaks correlated to zinc and oxygen and determines the atomic percentage of the elements present in the sample.

Figure 27 displays a high resolution scan centered on the peak corresponding to oxygen. The peak between 528 and 534 eV is a convolution of two peaks where the lower energy peak belongs to the O^{2-} anion electronic structure and the higher energy peak belongs to the OH^{-} anion electronic structure of oxygen. The area of the peaks is directly dependent on the atomic percentage of either of them in the sample.

The high resolution scan for nitrogen, between 390 and 410 eV, indicated that no nitrogen was present in the sample. This indicates that there is no lysine present in the sample after cleaning and annealing.

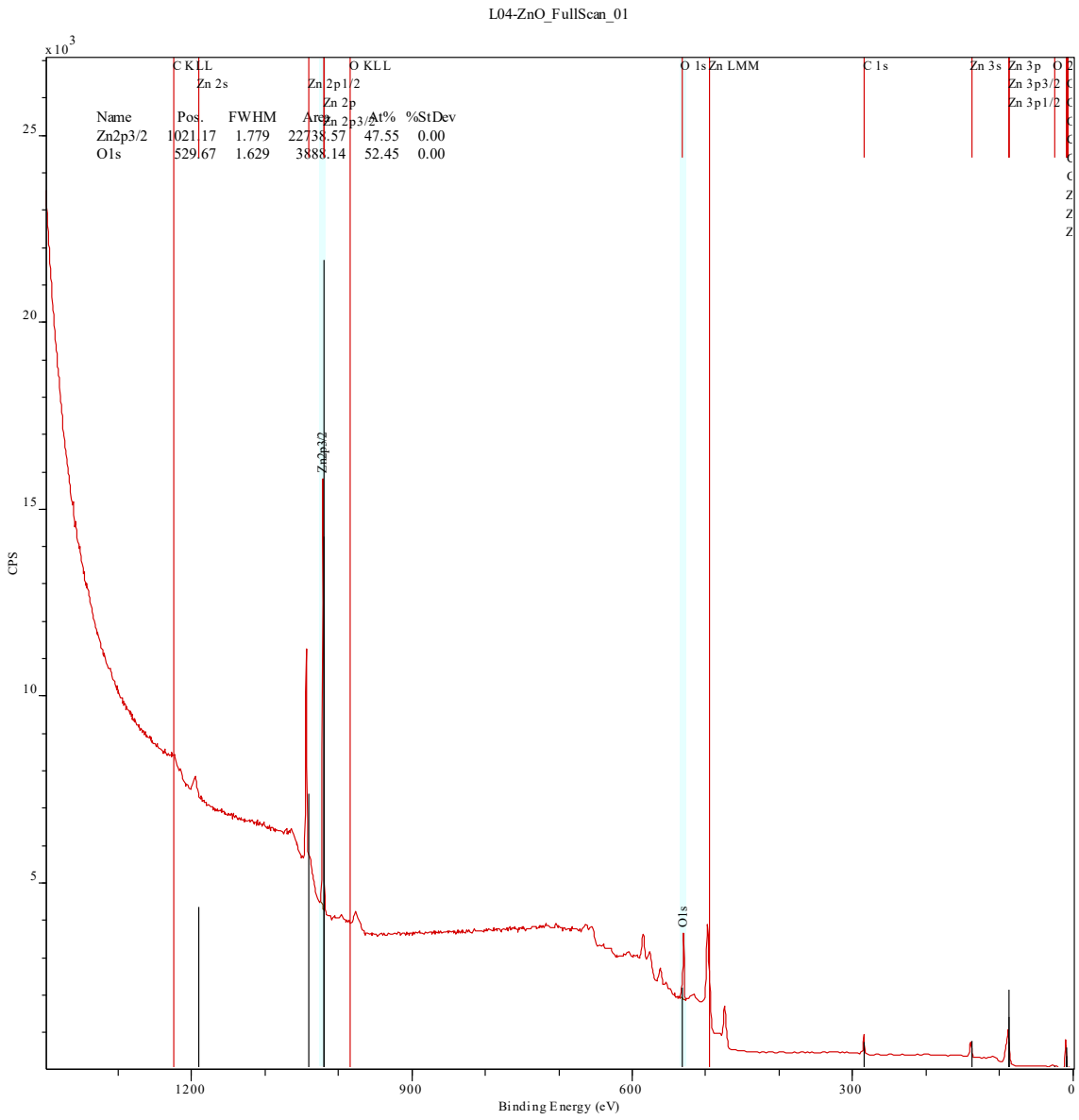

Figure 26: X-ray photoelectron spectroscopy full energy range scan where the vertical lines represent peaks corresponding to either zinc or oxygen atomic composition. The percentages in the top left corner correspond to measurements performed by CASA XPS to determine the atomic percentage of zinc and oxygen.

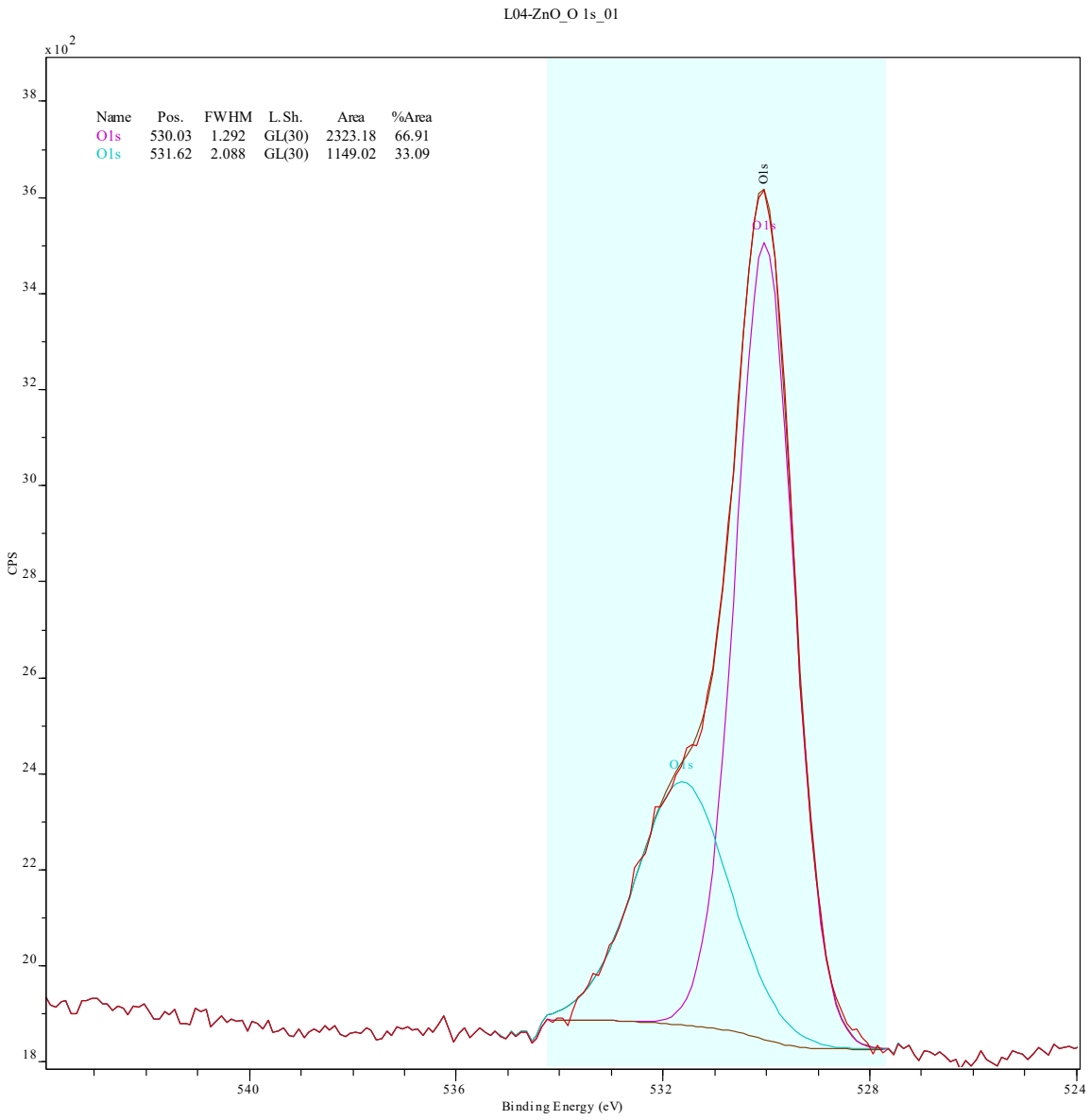

Figure 27: High resolution x-ray photoelectron spectroscopy scan over the peaks corresponding to oxygen. The left convoluted peak corresponds to OH^- oxygen states and the right peak corresponds to O^{2-} oxygen states.

Figure 28 and Figure 29 display the atomic percentage results from the CASA XPS analysis. Figure 28 displays the atomic percentage of zinc compared to oxygen present in the samples. Similar to EDX, with an increasing growth temperature, the atomic percentage approaches stoichiometry with a 50/50 atomic percentage. At lower

growth temperatures, the surface appears to have a higher concentration of oxygen atoms, but is not discernable enough between samples with and without lysine present during synthesis. Figure 29 displays the atomic percentage of O^{2-} anions present in the samples compared to OH^{-} anions. There does not appear to be a trend from the limited amount of data, but it can be seen that the surface varies considerably between temperatures and from the addition of lysine.

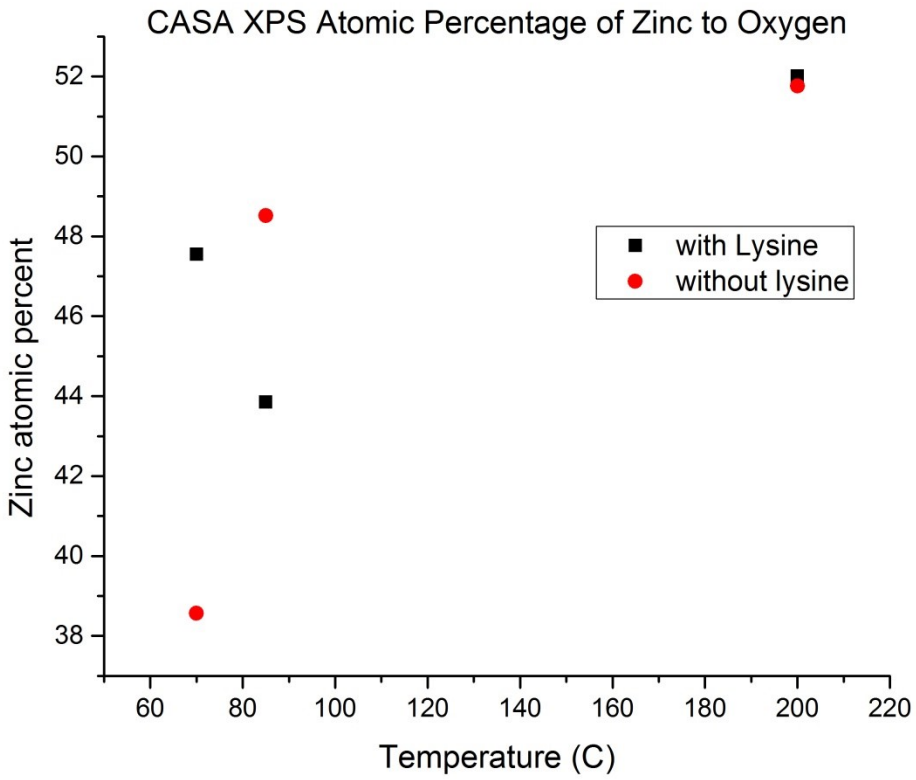

Figure 28: Zinc atomic percent when compared to oxygen atomic percent. The black dots correspond to samples with lysine while the red dots correspond to samples without lysine.

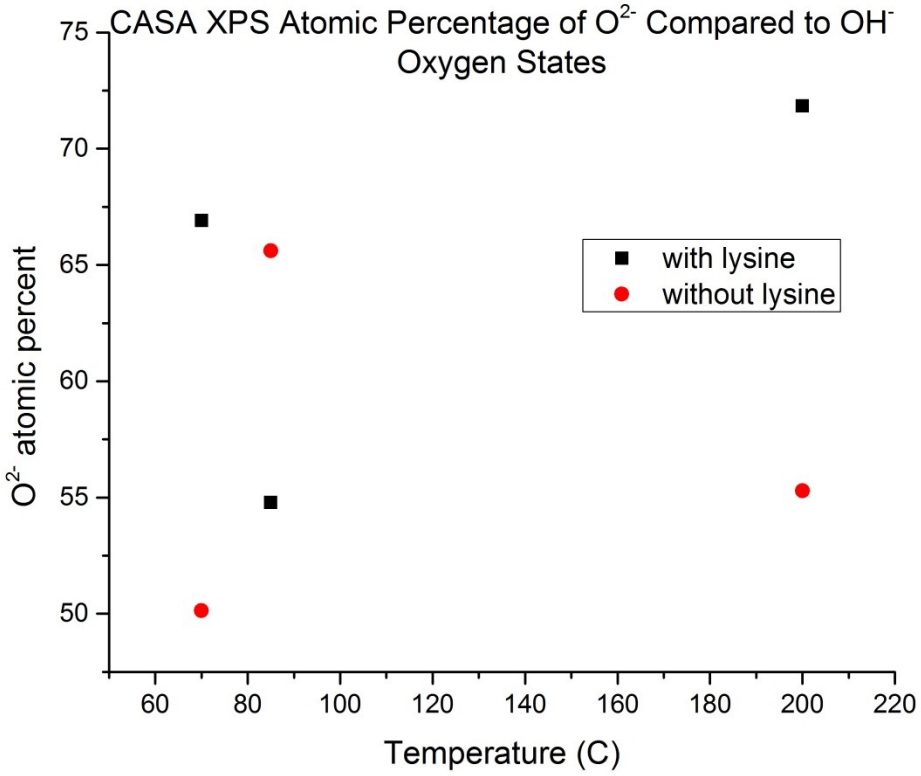

Figure 29: Atomic percent of O^{2-} oxygen states when compared to OH^- oxygen states. The black correspond to samples grown with lysine and the red dots correspond to samples grown without lysine.

CONCLUSION

The synthesis of zinc oxide nanoparticles was performed using the hydrothermal method. Molecule assisted hydrothermal synthesis was tested using L-lysine as a treatment molecule during the synthesis process. The molecule altered the size and shape of the nanoparticles generated at different growth temperatures as seen in the SEM images. It is clear that the molecule plays a large role in the growth kinetics during the formation of the nanomaterials. These changes alter the structural and optical properties of the nanoparticles.

The nanomaterials synthesized with lysine present all demonstrated changes in the atomic percentage of zinc to oxygen. The surface has a greater concentration of oxygen present when synthesized with lysine confirmed by both EDX and XPS results. The XRD results indicate a changing atomic percentage with and without lysine within the nanomaterial as well. Raman spectroscopy results indicate the enhancement of the A_1(TO) mode of vibration in the samples synthesized in the presence of lysine. This mode is c-axis mode of vibration and is not present in the samples without lysine.

The optical properties are greatly enhanced for the absorption of light. UV-Vis spectroscopy analysis indicates a decrease in the energy band gap of the nanomaterials synthesized with lysine and also an increased concentration of defect energy level states allowing for this enhancement in optical absorption properties. When compared to PL studies though, there only appears to be a slight red shift in the defect energy state peak of the zinc oxide nanomaterials.

This optical absorption enhancement would need to be further researched before the mechanism behind the enhancement can be understood. The possibility of using lysine as a treatment molecule in the hydrothermal method to alter the growth kinetics could be utilized in a number of ways to enhance zinc oxide as a material for solar energy applications. The possibilities of using treatment molecules in the hydrothermal method could be endless in the number of different materials and molecules available to alter any number of properties of the synthesized nanostructures.

REFERENCES

1. Antisari, M. V. *et al.* Low energy pure shear milling: A method for the preparation of graphite nano-sheets. *Scr. Mater.* **55,** 1047–1050 (2006).

2. Dutta, A. *et al.* Preparation of sol-gel nano-composites containing copper oxide and their gas sensing properties. *J. Sol-Gel Sci. Technol.* **26,** 1085–1089 (2003).

3. He, Q. & Shi, J. Mesoporous silica nanoparticle based nano drug delivery systems: synthesis, controlled drug release and delivery, pharmacokinetics and biocompatibility. *J. Mater. Chem.* **21,** 5845–5855 (2011).

4. O'Farrell, N., Houlton, A. & Horrocks, B. R. Silicon nanoparticles: Applications in cell biology and medicine. *Int. J. Nanomedicine* **1,** 451–472 (2006).

5. Cheng, K. *et al.* Magnetic nanoparticles: Synthesis, functionalization, and applications in bioimaging and magnetic energy storage. *Chem. Soc. Rev.* **38,** 2532–2542 (2009).

6. Lai, X., Halpert, J. E. & Wang, D. Recent advances in micro-/nano-structured hollow spheres for energy applications: From simple to complex systems. *Energy Environ. Sci.* **5,** 5604–5618 (2012).

7. Liu, C. & Cheng, H.-M. Carbon nanotubes for clean energy applications. *J. Phys. D. Appl. Phys.* **38,** R231–R252 (2005).

8. Lupan, O. *et al.* Well-aligned arrays of vertically oriented ZnO nanowires electrodeposited on ITO-coated glass and their integration in dye sensitized solar cells. *J. Photochem. Photobiol. A Chem.* **211,** 65–73 (2010).

9. Beek, W. J. E., Wienk, M. M. & Janssen, R. a. J. Efficient hybrid solar cells from zinc oxide nanoparticles and a conjugated polymer. *Adv. Mater.* **16,** 1009–1013 (2004).

10. Swart, H. C., Ntwaeaborwa, O. M., Mbule, P. S. & Dhlamini, M. S. P3HT: PCBM based solar cells: A short review focusing on ZnO nanoparticles buffer layer, post-fabrication annealing and an inverted geometry. *J. Mater. Sci. Eng.* **5,** 12–35 (2015).

11. Tsukazaki, A. *et al.* Repeated temperature modulation epitaxy for p-type doping and light-emitting diode based on ZnO. *Nat. Mater.* **4,** 42–46 (2004).

12. TSUKAZAKI, A. *et al.* Blue light-emitting diode based on ZnO. *Jpn. J. Appl. Phys.* **44,** L643–L645 (2005).

13. Gong, H., Hu, J. Q., Wang, J. H., Ong, C. H. & Zhu, F. R. Nano-crystalline Cu-

doped ZnO thin film gas sensor for CO. *Sensors Actuators, B Chem.* **115,** 247–251 (2006).

14. Sarala Devi, G., Bala Subrahmanyam, V., Gadkari, S. C. & Gupta, S. K. NH3 gas sensing properties of nanocrystalline ZnO based thick films. *Anal. Chim. Acta* **568,** 41–46 (2006).

15. Cho, P.-S., Kim, K.-W. & Lee, J.-H. NO2 sensing characteristics of ZnO nanorods prepared by hydrothermal method. *J. Electroceramics* **17,** 975–978 (2006).

16. Batista, P. D. & Mulato, M. ZnO extended-gate field-effect transistors as pH sensors. *Appl. Phys. Lett.* **87,** 1–3 (2005).

17. Kim, J., Park, W. & Lee, C. ZnO nanorod biosensor for highly sensitive detection of specific protein binding. *J. Korean Phys. Soc* **49,** 1635–1639 (2006).

18. Lu, Y., Emanetoglu, N. W. & Chen, Y. *ZnO piezoelectric devices*. *Zinc Oxide Bulk, Thin Films and Nanostructures* (2006). doi:10.1016/B978-008044722-3/50013-0

19. Emanetoglu, N. W. *et al.* Mg x Zn 1-x O : A new piezoelectric material. *IEEE Trans. Ultrason. Ferroelectr. Freq. Control* **50,** 537–543 (2003).

20. Özgür, Ü. *et al.* A comprehensive review of ZnO materials and devices. *J. Appl. Phys.* **98,** 1–103 (2005).

21. Baruah, S. & Dutta, J. Hydrothermal growth of ZnO nanostructures. *Sci. Technol. Adv. Mater.* **10,** 013001 (2009).

22. Burns, M. How Gallium Nitride Could Help Power the World. *Pacific Standard* (2013). at <http://www.psmag.com/books-and-culture/gallium-nitride-silicon-power-energy-55405>

23. Pan, Z. W., Dai, Z. R. & Wang, Z. L. Nanobelts of semiconducting oxides. *Science (80-.).* **291,** 1947–1949 (2001).

24. Dalal, S. H. *et al.* Controllable growth of vertically aligned zinc oxide nanowires using vapour deposition. *Nanotechnology* **17,** 4811–4818 (2006).

25. Li, Z. W. & Gao, W. Growth of zinc oxide thin films and nanostructures by wet oxidation. *Thin Solid Films* **515,** 3323–3329 (2007).

26. Spanhel, L. Colloidal ZnO nanostructures and functional coatings: A survey. *J. Sol-Gel Sci. Technol.* **39,** 7–24 (2006).

27. Shingubara, S. Fabrication of nanomaterials using porous templates. *J. Nanoparticle Res.* **5,** 17–30 (2003).

28. Lee, J.-H., Leu, I.-C., Chung, Y.-W. & Hon, M.-H. Fabrication of ordered ZnO hierarchical structures controlled via surface charge in the electrophoretic deposition process. *Nanotechnology* **17,** 4445–4450 (2006).

29. Ma, X., Zhang, H., Ji, Y., Xu, J. & Yang, D. Sequential occurrence of ZnO nanopaticles, nanorods, and nanotips during hydrothermal process in a dilute aqueous solution. *Mater. Lett.* **59,** 3393–3397 (2005).

30. Amin, G. *et al.* Influence of pH, Precursor Concentration, Growth Time, and Temperature on the Morphology of ZnO Nanostructures Grown by the Hydrothermal Method. *J. Nanomater.* **2011,** 1–9 (2011).

31. Baruah, S., Thanachayanont, C. & Dutta, J. Growth of ZnO nanowires on nonwoven polyethylene fibers. *Sci. Technol. Adv. Mater.* **9,** 025009 (2008).

32. Huang, Y. *et al.* Bicrystalline zinc oxide nanocombs. *J. Nanosci. Nanotechnol.* **6,** 2566–2570 (2006).

33. Hughes, W. L. & Wang, Z. L. Controlled synthesis and manipulation of ZnO nanorings and nanobows. *Appl. Phys. Lett.* **86,** 84–87 (2005).

34. Kong, X. Y. & Wang, Z. L. Spontaneous polarization-induced nanohelixes, nanosprings, and nanorings of piezoelectric nanobelts. *Nano Lett.* **3,** 1625–1631 (2003).

35. Sun, T., Qui, J. & Liang, C. Controllable fabrication and photocatalytic activity of ZnO nanobelt arrays. *J. Phys. Chem. C* **112,** 715–721 (2008).

36. Snure, M. & Tiwari, A. Synthesis, characterization, and green luminescence in ZnO nanocages. *J. Nanosci. Nanotechnol.* **7,** 481–485 (2007).

37. Wang, Z. L. Zinc oxide nanostructures: Growth, properties and applications. *J. Phys. Condens. Matter* **16,** R829–R858 (2004).

38. Calleja, J. & Cardona, M. Resonant Raman scattering in ZnO. *Phys. Rev. B* **16,** 3753–3761 (1977).

39. Emelie, P. Y., Phillips, J. D., Buller, B. & Venkateswaean, U. D. Free carrier absorption and lattice vibrational modes in bulk ZnO. *J. Electron. Mater.* **35,** 525–529 (2006).

40. Arguello, C., Rousseau, D. & Porto, S. First-Order Raman Effect in Wurtzite-Type Crystals. *Phys. Rev.* **181,** 1351–1363 (1969).

41. Zeng, H. *et al.* Blue luminescence of ZnO nanoparticles based on non-equilibrium processes: Defect origins and emission controls. *Adv. Funct. Mater.* **20,** 561–572 (2010).

42. Xu, P. S., Sun, Y. M., Shi, C. S., Xu, F. Q. & Pan, H. B. The electronic structure and spectral properties of ZnO and its defects. *Nucl. Instruments Methods Phys. Res. Sect. B Beam Interact. with Mater. Atoms* **199,** 286–290 (2003).

43. Stehr, J. E. *et al.* Defects in N, O and N, Zn implanted ZnO bulk crystals. *J. Appl. Phys.* **113,** 103509 (2013).

44. Kohan, a. F., Ceder, G., Morgan, D. & Van de Walle, C. G. First-principles study of native point defects in ZnO. *Phys. Rev. B* **61,** 15019–15027 (2000).

45. Van De Walle, C. G. Defect analysis and engineering in ZnO. *Phys. B* **308-310,** 899–903 (2001).

46. Van De Walle, C. G. Hydrogen as a cause of doping in zinc oxide. *Phys. Rev. Lett.* **85,** 1012–1015 (2000).

47. Janotti, A. & Van de Walle, C. G. Hydrogen multicentre bonds. *Nat. Mater.* **6,** 44–47 (2007).

48. Mbamara, U. S. Deposition and characterisation of nitrogen-doped zinc oxide thin films by MOCVD using zinc acetate—ammonium acetate precursor. *J. Mod. Phys.* **03,** 652–659 (2012).

49. Samanta, P. K. & Chaudhuri, P. R. Substrate effect on morphology and photoluminescence from ZnO monopods and bipods. *Front. Optoelectron. China* **4,** 130–136 (2011).

50. Byrappa, K. & Yoshimura, M. *Handbook of hydrothermal technology.pdf*. (Noyes Publications, 2001).

51. Hayashi, H. & Hakuta, Y. Hydrothermal synthesis of metal oxide nanoparticles in supercritical water. *Materials (Basel).* **3,** 3794–3817 (2010).

52. Shen, L. *et al.* Organic molecule-assisted hydrothermal self-assembly of size-controlled tubular ZnO nanostructures. *J. Phys. Chem. C* **111,** 7280–7287 (2007).

53. Zhang, H., Yang, D., Li, D., Ma, Xiangyang Li, S. & Que, D. Controllable growth of ZnO microcrystals by a capping-molecule-assisted hydrothermal process. *Cryst. Growth Des.* **5,** 547–550 (2005).

54. Liu, S.-J., Gong, J.-Y., Hu, B. & Yu, S.-H. Mesocrystals of rutile TiO2: Mesoscale transformation, crystallization, and growth by a biologic molecules-assisted hydrothermal process. *Cryst. Growth Des.* **9,** 203–209 (2009).

55. Zhang, J., Sun, Y., Yao, Y., Huang, T. & Yu, A. Lysine-assisted hydrothermal synthesis of hierarchically porous Fe2O3 microspheres as anode materials for lithium-ion batteries. *J. Power Sources* **222,** 59–65 (2013).

56. Liu, J. *et al.* Enhanced photoconduction of free-standing ZnO nanowire films by L-lysine treatment. *Nanotechnology* **21,** 485504 (2010).

57. Tao, M., Zhu, M., Wu, C. & He, Z. Degradation kinetic study of lysine in lysine hydrochloride solutions for injection by determining its main degradation product. *Asian J. Pharm. Sci.* **10,** 57–63 (2015).

58. Ohara, S., Mousavand, T., Umetsu, M., Takami, S. & Adschiri, T. Hydrothermal synthesis of fine zinc oxide nano-particles under supercitical conditions. *Solid State Ionics* **172,** 261–264 (2004).

59. Kuo, C.-L., Kuo, T.-J. & Huang, M. Hydrothermal synthesis of ZnO microspheres and hexagonal microrods with sheetlike and platelike nanostructures. *J. Phys. Chem. B* **109,** 20115–20121 (2005).

60. Lin, M. S., Chen, C. C., Wang, W. C., Lin, C. F. & Chang, S. Y. Fabrication of the selective-growth ZnO nanorods with a hole-array pattern on a p-type GaN:Mg layer through a chemical bath deposition process. *Thin Solid Films* **518,** 7398–7402 (2010).

61. Liu, B. & Zeng, H. C. Hydrothermal synthesis of ZnO nanorods in the diameter regime of 50 nm. *J. Am. Chem. Soc.* **125,** 4430–4431 (2003).